

Investigation of Total Collision Energy and Underlying Event Activity via Transverse Energy  
Measurements in Au+Au and p+p collisions at 200 GeV with the sPHENIX Detector

Emma McLaughlin

Submitted in partial fulfillment of the  
requirements for the degree of  
Doctor of Philosophy  
under the Executive Committee  
of the Graduate School of Arts and Sciences

COLUMBIA UNIVERSITY

2026

© 2026

Emma McLaughlin

All Rights Reserved

## Abstract

# Investigation of Total Collision Energy and Underlying Event Activity via Transverse Energy

## Measurements in Au+Au and p+p collisions at 200 GeV with the sPHENIX Detector

# Emma McLaughlin



problem of the thesis/dissertation, (2) discuss the materials and methods used, and (3) state the conclusions reached. Individual chapters should not have abstracts.

## Table of Contents

Acknowledgments . . . . .	viii
Dedication . . . . .	ix
Introduction or Preface . . . . .	1
Chapter 1: Introduction and Background . . . . .	2
1.1 Footnotes: Two ways of adding to your text . . . . .	2
1.2 Other section of first chapter . . . . .	2
Chapter 2: Experimental Detector Design . . . . .	3
2.1 Relativistic Heavy Ion Collider . . . . .	3
2.2 sPHENIX Detector . . . . .	4
2.2.1 sPHENIX Tracking System . . . . .	6
2.2.2 sPHENIX Calorimeter System . . . . .	13
2.2.3 sPHENIX Global Detectors . . . . .	16
2.2.4 sPHENIX Data Acquisition and Readout . . . . .	19
Chapter 3: sPHENIX Calorimeter Commissioning, Reconstruction and Calibration . . . . .	23
3.1 Real-time Calorimeter State Logging and Monitoring . . . . .	23
3.2 sPHENIX Low-Level Data Reconstruction . . . . .	27

3.2.1	Diagnosing ADC Bit Issues . . . . .	27
3.2.2	Online ADC Firmware Fixes . . . . .	28
3.2.3	Offline Reconstruction Software Fixes . . . . .	30
3.3	sPHENIX Calorimeter Calibration and Reconstruction Routines . . . . .	33
3.3.1	Calorimeter Tower Reconstruction . . . . .	33
3.3.2	EMCal Energy Calibration . . . . .	34
3.3.3	HCal Energy Calibration . . . . .	44
3.3.4	Calorimeter Zero Suppression and Cross Calibration . . . . .	46
Chapter 4:	Transverse Energy Density Measurements in Au+Au Collisions . . . . .	61
Chapter 5:	Underlying Event Measurements in p+p Collisions . . . . .	62
Chapter 6:	Last Chapter before conclusion . . . . .	63
Conclusion or Epilogue . . . . .	64	
References . . . . .	65	
Appendix A:	Experimental Equipment . . . . .	67
Appendix B:	Data Processing . . . . .	68

## List of Figures

2.1 Schematic of RHIC acceleration chain for Au beams. Reproduced from [1]. . . . .	5
2.2 Diagram of full array of sPHENIX physics program goals including measurements in jet structure, heavy flavor, quarkonia, bulk heavy ion physics and proton spin physics. . . . .	5
2.3 sPHENIX detector with subsystems labeled. . . . .	7
2.4 (a) Schematic of an sPHENIX MVTX stave (left) and half barrel layer made up of staves and service section (right). (b) Cross-section of MVTX silicon barrel with its 3 layers highlighted in different colors (Red, Green, and Blue) and sPHENIX beam pipe included to highlight the MVTX location relative to the beam pipe. Reproduced from [3]. . . . .	9
2.5 Schematic of sPHENIX INTT silicon ladder component. Highlighted on silicon ladder are silicon sensors, readout chips and high-density interconnect (HDI) cables. Reproduced from [6]. . . . .	10
2.6 Left: Cross-section schematic of sPHENIX TPC showing central membrane (CM), inner- and outer-field cages (I-FC, O-FC) and end plates (EP). Middle: Segmentation of TPC endcap into 72 GEM modules. Right: Schematic of TPC GEM modules highlighting the four foil layers with varying electric fields and pad plane for readout of amplified signal. Reproduced from [7]. . . . .	11
2.7 (a) Schematic of sPHENIX TPOT detector (left). (b) Schematic of track reconstruction using all tracking subsystems highlighting the benefit to having a TPOT hit for drift corrections. (c) Cross-section of TPOT Micromegas chamber. Reproduced from [9]. . . . .	12
2.8 (a) Photo of the sPHENIX EMCal, IHCAL and OHCal detectors after installation and cabling. (b) Graphic of sPHENIX IHCAL (red), OHCal (gray) and superconducting magnet (pink) from GEANT simulation. IHCAL(OHCal) scintillator tiles shown in yellow(green). . . . .	14
2.9 (a) Schematic of EMCal sector highlighting projective geometry of towers in $\eta$ and lightguides and electronics on the inner radius of the sector. (b) Schematic of OHCal half-sector highlighting projective geometry of towers in $\eta$ , layered absorber/scintillator tile tower design, wavelength-shifting fiber located within HCal scintillating tiles, and readout electronics on the outer radius of the sector. Reproduced from [7]. . . . .	15
2.10 Left: Schematic of 64 MBD module array mounted on detector frame. Right: Photo of individual MBD module with quartz radiator and PMT. Reproduced from [7]. . . . .	17

2.11 Schematic of sPHENIX ZDC detector shown from (a) collision region view and (b) "beam's eye" view to show the ZDC location past the RHIC DX dipole magnets and between the beam pipes. Also shown is the trajectory of beam fragments with neutrons measured in the region of the ZDC and protons deflected. Reproduced from [14]. . . . .	18
2.12 Flowchart of sPHENIX data aquisition system showing progagation through the stages of data aquisition from the front end electronics to the RHIC computing facility. Reproduced from [7]. . . . .	20
2.13 Detailed flowchart of sPHENIX data aquisition system for triggered subsystems (calorimeters and global detectors) including feedback on data readout from Trigger System. Reproduced from [7]. . . . .	21
3.1 (a) Diagram of EMCal sector design with interface board connections to slow control, MPOD, low voltage power and ADC boards. (b) Diagram of HCal half-sector design with interface board connections to slow control, MPOD, low voltage power and ADC boards. Reproduced from [7]. . . . .	24
3.2 Diagram of HCal database table schema for logging detector state information. Includes tables for hcal slow control and bias voltage information as well as LED and pedestal run analysis results. . . . .	25
3.3 (a) Shifter monitoring dashboard for HCal gain, SiPM temperature and bias voltage offsets, LED and Pin Diode status. (b) Bias voltage monitoring dashboard showing the bias voltage for sector of the HCal. . . . .	26
3.4 Diagram of the ADC board design used for digitization of signals from the sPHENIX calorimeters. Reproduced from [7]. . . . .	28
3.5 Examples of abnormal waveforms with bit flip (top) or $2^n$ gaps of ADC counts (middle and bottom) behavior. Left plots show the abnormal waveforms for a single event. Right plot show a peristancy plot of the channels waveforms overlaid for an entire run. . . . .	29
3.6 (a) Diagram of shifted bit-stream read out for a single ADC channel in the case of mis-alignment during ADC configuration step. (b) Examples of abnormal shifted bit-stream waveforms in red and waveforms after re-shifted recovery procedure in blue. Right figures included to show re-shifted waveforms in detail. . . . .	31
3.7 Pseudo-code algorithm for discovering and recovering calorimeter waveforms digitized with stuck high value bits using the quality of fit to the calorimeter waveform template. . . . .	32
3.8 Example waveforms of before (left) and after (right) the waveform recovery method for an EMCAL channel with a known intermittent stuck bit $2^{11}$ . . . . .	33
3.9 EMCAL di-cluster invariant mass distribution from Run 2024 Au+Au data (black points) and geant-4 simulation of HIJING events (blue histogram) before cluster energy smearing. . . . .	36
3.10 EMCAL $\pi^0$ mass peak position (top) and relative width (bottom) for simulation (red), simulation with cluster energy smearing (green), data calibrated to the un-smeared simulation (blue) and data calibrated to the smeared simulation (black). Left plots show quantities as a function of cluster $\eta$ slice and right plots show the $\eta$ averaged quantities for easy comparison. . . . .	38

3.11 Final EMCAL di-cluster invariant mass distribution from Run 2024 Au+Au data (black points) and geant-4 simulation of HIJING events (blue histogram). . . . .	39
3.12 EMCAL $\pi^0$ mass peak position (left) and relative width (right) as a function of $\pi^0 p_T$ for simulation (red), simulation with cluster energy smearing (pink), data calibrated to the un-smeared simulation (blue) and data calibrated to the smeared simulation (black). . . . .	39
3.13 EMCAL di-cluster invariant mass distributions for bins of $\pi^0 p_T$ for simulation (left), simulation with cluster energy smearing (left middle), data calibrated to the un-smeared simulation (right middle) and data calibrated to the smeared simulation (right). Fits to the $\pi^0$ mass peak using Gaussian plus polynomial background are included. . . . .	40
3.14 Left: Ratio of EMCAL tower energies with and without inclusion of realistic EMCAL tower noise as a function of EMCAL tower energies without inclusion of realistic EMCAL tower noise. Right: Profile of ratio of EMCAL tower energies with and without inclusion of realistic EMCAL tower noise for EMCAL tower energies around 1 GeV. . . . .	41
3.15 EMCAL $\pi^0$ mass peak position value (left) and variation from nominal (right) as a function of $\eta$ for nominal result (red), variations in cluster tower energy thresholds (green, blue), and variation in simulation centrality selection (yellow). Variation results for simulation are shown in top plots and for data are shown in bottom plots. . . . .	42
3.16 EMCAL $\pi^0$ mass peak relative width value (left) and variation from nominal (right) as a function of $\eta$ for nominal result (red), variations in cluster tower energy thresholds (green, blue), and variation in simulation centrality selection (yellow). Variation results for simulation are shown in top plots and for data are shown in bottom plots. . . . .	43
3.17 Comparison of OHCal tower MIP energy distribution from cosmic ray data (black) and GEANT-4 simulation of EcoMug generated cosmic ray muons (blue histogram) for an example tower used in the absolute energy scale calibration. The characteristic MIP peak is clearly visible around 250 MeV. . . . .	45
3.18 Comparison of EMCAL waveform processing with zero suppression versus template fit. Correlation between tower's ADC value from ZS versus from template fit shown in left plots for two different ADC ranges [-100,1000] ADC (top left) and [-100,100] ADC (bottom left). Ratio of ADC value from ZS versus ADC value from template fit on a tower by tower basis shown in right plots for two different ranges [100,1000] ADC (top right) and [-100,100] ADC (bottom right). . . . .	47
3.19 Comparison of OHCal waveform processing with zero suppression versus template fit. Correlation between tower's ADC value from ZS versus from template fit shown in left plots for two different ADC ranges [-100,1000] ADC (top left) and [-100,100] ADC (bottom left). Ratio of ADC value from ZS versus ADC value from template fit on a tower by tower basis shown in right plots for two different ranges [100,1000] ADC (top right) and [-100,100] ADC (bottom right). . . . .	48

3.20 Comparison of IHCAL waveform processing with zero suppression versus template fit. Correlation between tower's ADC value from ZS versus from template fit shown in left plots for two different ADC ranges [-100,1000] ADC (top left) and [-100,100] ADC (bottom left). Ratio of ADC value from ZS versus ADC value from template fit on a tower by tower basis shown in right plots for two different ranges [100,1000] ADC (top right) and [-100,100] ADC (bottom right). . . . .	49
3.21 Examples of noisy waveforms from beam data. . . . .	51
3.22 EMCal, IHCAL and OHCal total total $E_T$ distributions with ZS cross calibration factors applied for 5 different ZS thresholds. Plots made with ana.403 p011 production	55
3.23 Comparison of reconstructed EMCal $dE_T/d\eta$ measurements (top) and ratios to full template fit EMCal $dE_T/d\eta$ (bottom) from beam data processed using ZS + template fit method for thresholds between 10 and 50 ADC with (left) and without (right) tower by tower ZS cross calibration factors applied. . . . .	56
3.24 Comparison of reconstructed IHCAL $dE_T/d\eta$ measurements (top) and ratios to full template fit IHCAL $dE_T/d\eta$ (bottom) from beam data processed using ZS + template fit method for thresholds between 10 and 50 ADC with (left) and without (right) tower by tower ZS cross calibration factors applied. . . . .	57
3.25 Comparison of reconstructed OHCal $dE_T/d\eta$ measurements (top) and ratios to full template fit OHCal $dE_T/d\eta$ (bottom) from beam data processed using ZS + template fit method for thresholds between 10 and 50 ADC with (left) and without (right) tower by tower ZS cross calibration factors applied. . . . .	58
3.26 Comparison of reconstructed-level $dE_T/d\eta$ from pedestal data processed using template fit only and ZS + template fit method for different ZS thresholds. Plots in right column are included to more clearly show the results included in the center column plots with values close to zero. . . . .	59

## **List of Tables**

1.1 This is an example Table. . . . .	2
---------------------------------------	---

## **Acknowledgements**

Insert your acknowledgements text here. This page is optional, you may delete it if not needed.

## **Dedication**

Insert your dedication text here. This page is optional, you may delete it if not needed.

## **Introduction or Preface**

Insert your preface text here if applicable. This page is optional, you may delete it if not needed. If you delete this page make sure to move page counter comment in thesis.tex to correct location.

# **Chapter 1: Introduction and Background**

## **1.1 Footnotes: Two ways of adding to your text**

<sup>1</sup>. Or it is possible to mark the location of a foot note with footnote mark command<sup>2</sup> then you can write the footnote in its own line for ease of reading.

## **1.2 Other section of first chapter**

---

<sup>1</sup>By using footnote command and writing your note in the curly brackets

<sup>2</sup>You then use footnotetext command and then write you note in as if you are using regular footnote command as we did previously.

Table 1.1: This is an example Table.

x	f(x)	g(x)
1	6	4
2	6	3
3	6	2
4	6	2

## Chapter 2: Experimental Detector Design

### 2.1 Relativistic Heavy Ion Collider

The Relativistic Heavy Ion Collider (RHIC) is a hadron accelerator located at Brookhaven National Lab (BNL) in Upton, NY capable of colliding a range of ion species from protons to uranium at center of mass energies as high as 500 GeV. RHIC can collide Au ions at center of mass energies of 7.7 GeV to 200 GeV per nucleon pair and protons at energies of 200 GeV to 500 GeV. During 2024, RHIC provided both proton-proton and Au+Au collisions at 200 GeV and sPHENIX's collected datasets from these collision systems are used in measurements presented in Chapters 4 and 5.

RHIC is comprised of two quasi-circular concentric storage rings of circumference 3.8 km. Each ring has six 356 m long arc sections and six 277 m long insertion sections, which each contain a collision point at their center enabling six interaction points for the two rings [1]. The two rings are labeled "blue" for counter-clockwise beam and "yellow" for clockwise beam. The arc sections are each composed of 11 focusing quadrupole, drift space, defocusing quadrupole, drift space (FODO) cells and the beams are separated by 90 cm horizontally within the arc sections. In the insertion sections, a pair of dipole magnets are used to steer the beams and three quadropole magnets are used to focus the beams for high luminosity head-on collision in the collision points. In total, 1740 superconducting magnets were required for the two storage rings.

To reach a stage of steady ion storage and collision at RHIC, a series of ion sources and accelerators are needed [1]. When running with heavy ions such as Au, ions are first produced from the Electron Beam Ion Source (EBIS), which is an upgrade from the Tandem Van de Graaff previous used as the heavy ion source for RHIC operations [2]. In the EBIS, Au atoms are ionized via electron-impact ionization, freeing the atoms' bound-state electrons until  $Au^{32+}$  ions are created.

Following the EBIS, ions are injected into the Booster Synchrotron which accelerates the ions to an energy of 95 MeV/u. When exiting the Booster, ions are stripped again, this time via a silicon foil to reach a ionization of  $Au^{77+}$ , reaching a Helium-like ionization. The ions are then injected into the Alternating Gradient Synchrotron (AGS) for further acceleration to 10.8 GeV/u. The ions enter the AGS in 24 bunches and are then de-bunched and re-bunched into four bunches for acceleration in the AGS. These four bunches are then ejected individually into the AGS-to-RHIC (ATR) beam transfer line and ions in these bunches are stripped of their remaining two electrons in the ATR via another stripping foil. The fully stripped  $Au^{79+}$  ions are split across the two beams and organized into buckets via a switching magnet at the end of the ATR transfer line. Finally, the magnets in RHIC's storage and accelerator rings are used to steer and focus the beams as they are accelerated to their final energies of 100 GeV/u.

The ion production and acceleration chain for proton-proton collisions is similar. However, in the proton case, protons are sourced from a hydrogen gas source and first accelerated using a linear accelerator (LINAC) before entering the Booster → AGS → ATR → RHIC chain [1]. Figure 2.1 shows a schematic of the ionization and acceleration process for creating RHIC Au ion beams.

## 2.2 sPHENIX Detector

The super Pioneering High Energy Nuclear Interaction eXperiment (sPHENIX) detector is located at RHIC and employs an array of central tracking, calorimeter and global event characterization subsystems in order to make measurements of the heavy ion and proton-proton collisions that occur from the RHIC beams. sPHENIX is the first general purpose detector to be built on a particle collider in the last decade and has been built with specific goals of measuring jets, heavy flavor and quarkonia at RHIC energies for direct comparison with measurements in the last decade from the LHC experiments. The full array of sPHENIX physics program goals can be found in Fig. 2.2.

sPHENIX began data taking in 2023 with a commissioning dataset of Au+Au collisions at  $\sqrt{s_{NN}} = 200$  GeV. In 2024, sPHENIX took its premire physics dataset of  $p+p$  collisions at

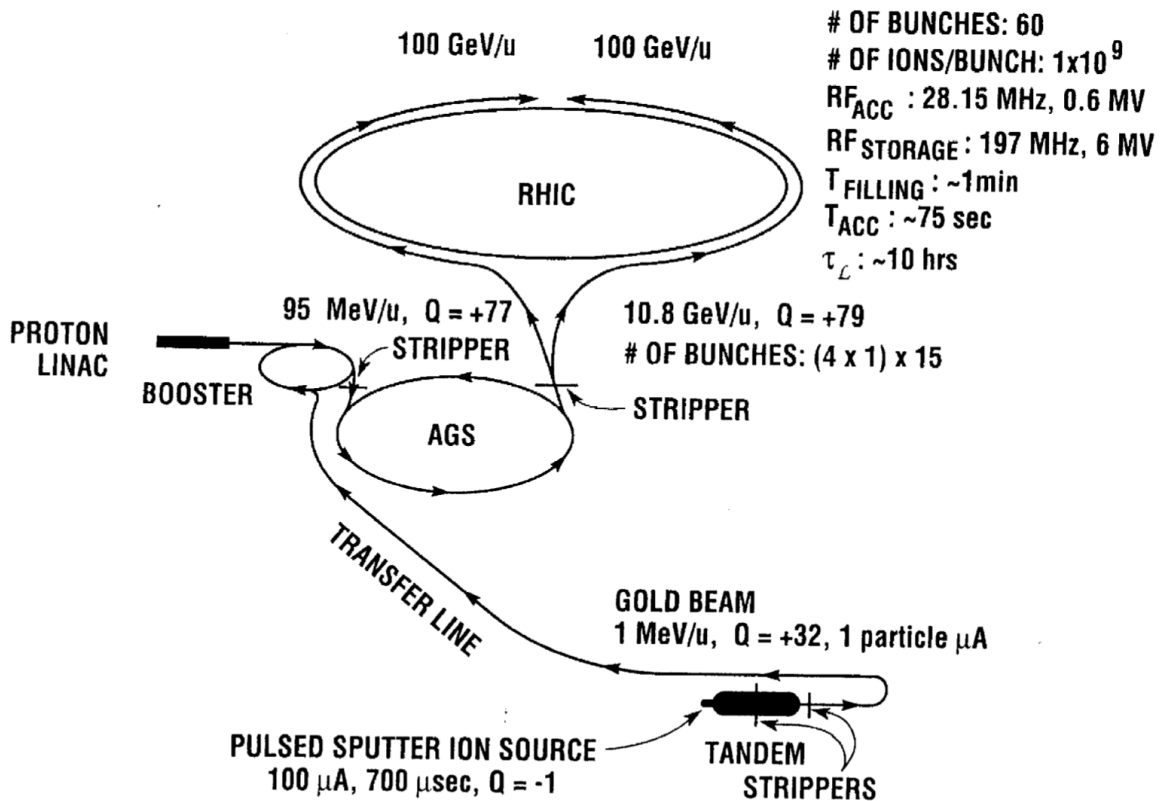


Figure 2.1: Schematic of RHIC acceleration chain for Au beams. Reproduced from [1].

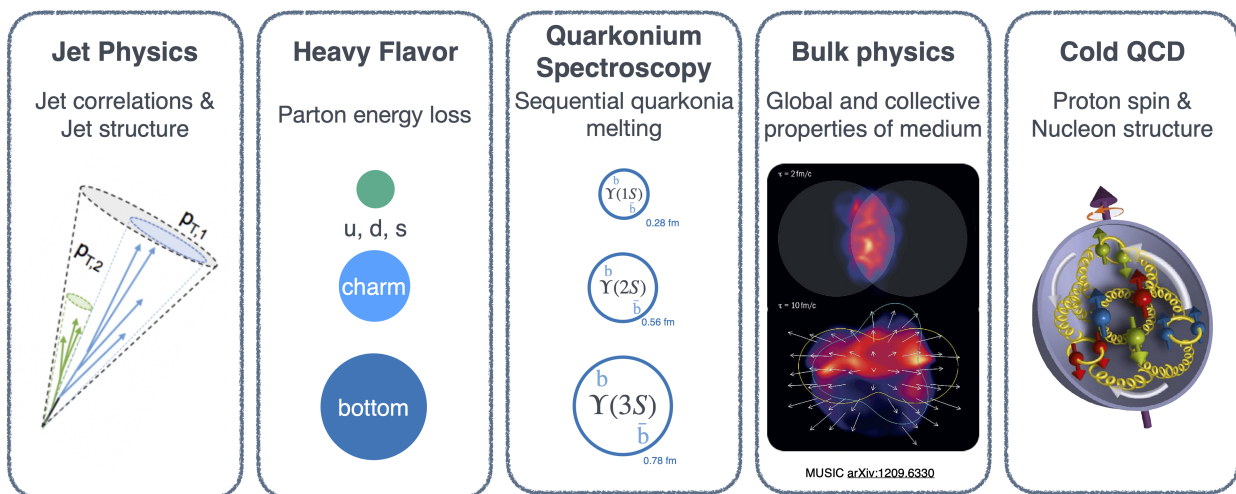


Figure 2.2: Diagram of full array of sPHENIX physics program goals including measurements in jet structure, heavy flavor, quarkonia, bulk heavy ion physics and proton spin physics.

$\sqrt{s} = 200$  GeV sampling over  $100 \text{ pb}^{-1}$  allowing for precision jet measurements in  $p+p$  collisions at RHIC energies. sPHENIX also collected an additional dataset of Au+Au collisions at  $\sqrt{s_{NN}} = 200$  GeV in 2024 intended for the commissioning of the tracking detectors with the calorimeter system and global detectors in full physics datataking mode. This Au+Au dataset was very useful in validating the calorimeter and jet reconstruction, calibration and performance and provided confidence in the sPHENIX data collection and reconstruction prior to the sPHENIX high statistics flagship Au+Au dataset collected in 2025 sampling  $7 \text{ nb}^{-1}$ . The results shown in this thesis are from the 2024  $p+p$  and Au+Au datasets.

sPHENIX has three main subsystem groups: a 4-part tracking system with a MAPS-based vertex detector (MVTX), an intermediate silicon tracker (INTT), the time projection chamber (TPC) and the TPC Outer Tracker (TPOT), a central barrel calorimeter system with three calorimeter layers of electromagnetic and hadronic calorimetry (EMCal, IHCal and OHCal), and global detectors including the Minimum Bias Detector (MBD), Zero Degree Calorimeters (ZDCs) and sPHENIX Event Plane Detector (sEPD). A rendering of the sPHENIX detector highlighting these subsystems with labels can be found in Fig. 2.3.

### 2.2.1 sPHENIX Tracking System

The sPHENIX tracking system comprises four subdetectors: a MAPS-based vertex detector (MVTX), an intermediate silicon tracker (INTT), the time projection chamber (TPC) and the TPC Outer Tracker (TPOT). These tracking subdetectors can provide a combination of particle momentum measurements, particle species identification, and secondary vertex reconstruction for use in physics measurements especially related to heavy flavor physics and jet substructure.

The MVTX is the innermost tracking subsystem, at a distance of 2 to 5 cm from the beam pipe, and is a 3 layer silicon barrel design with full azimuthal coverage ( $0 < \phi < 2\pi$ ) and pseudorapidity coverage of  $|\eta| < 1$ . Each layer of silicon barrel is composed of a set of staves, for a total of 48 staves, which each contain a hybrid integrated circuit with a flexible printed circuit connected to nine ALICE Pixel Detector (ALPIDE) pixel chip sensors, for a total of 432 ALPIDE sensors [3,

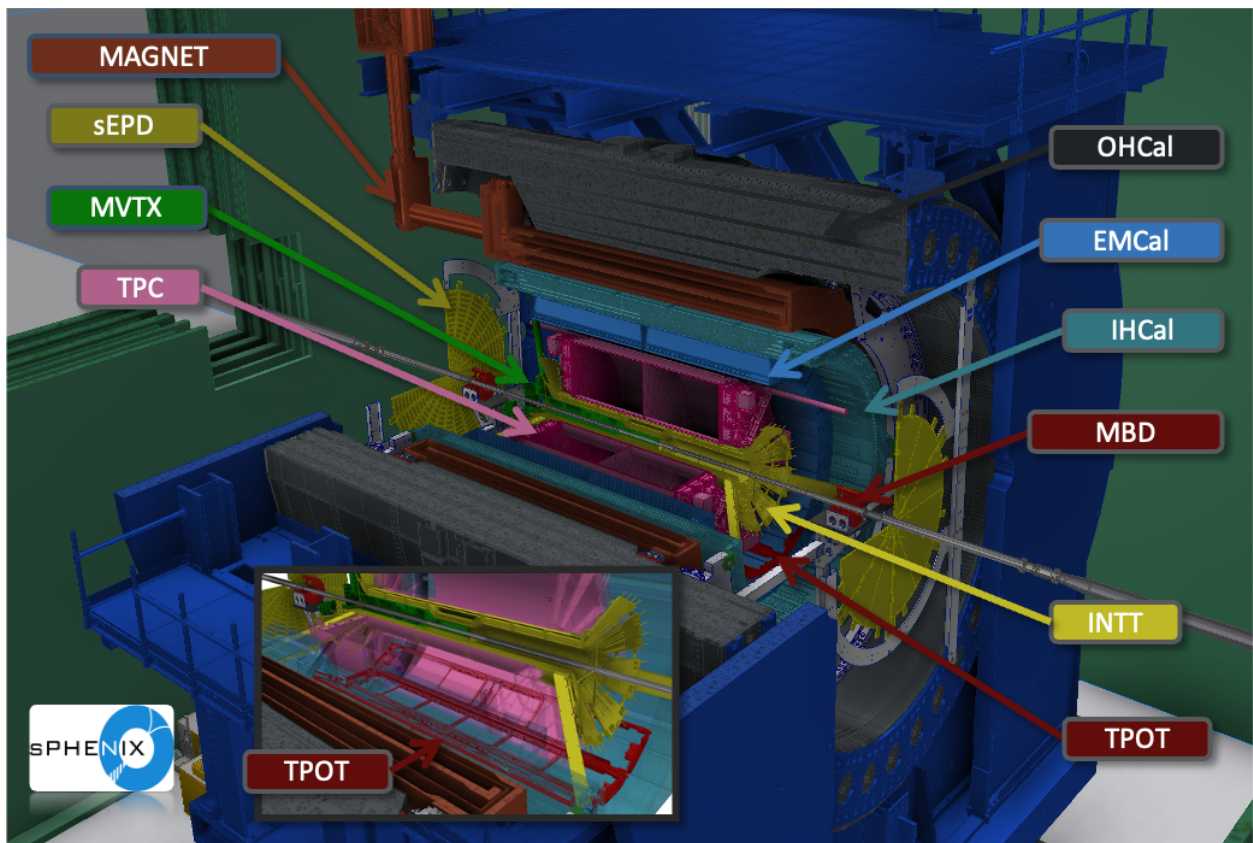
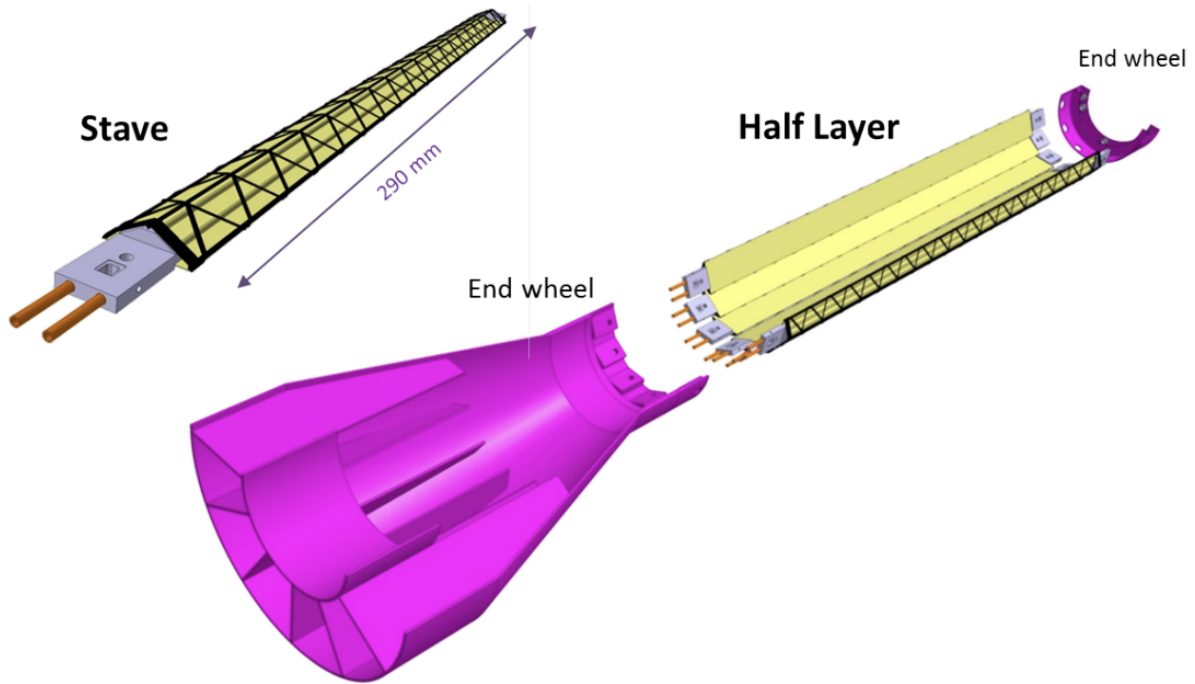


Figure 2.3: sPHENIX detector with subsystems labeled.

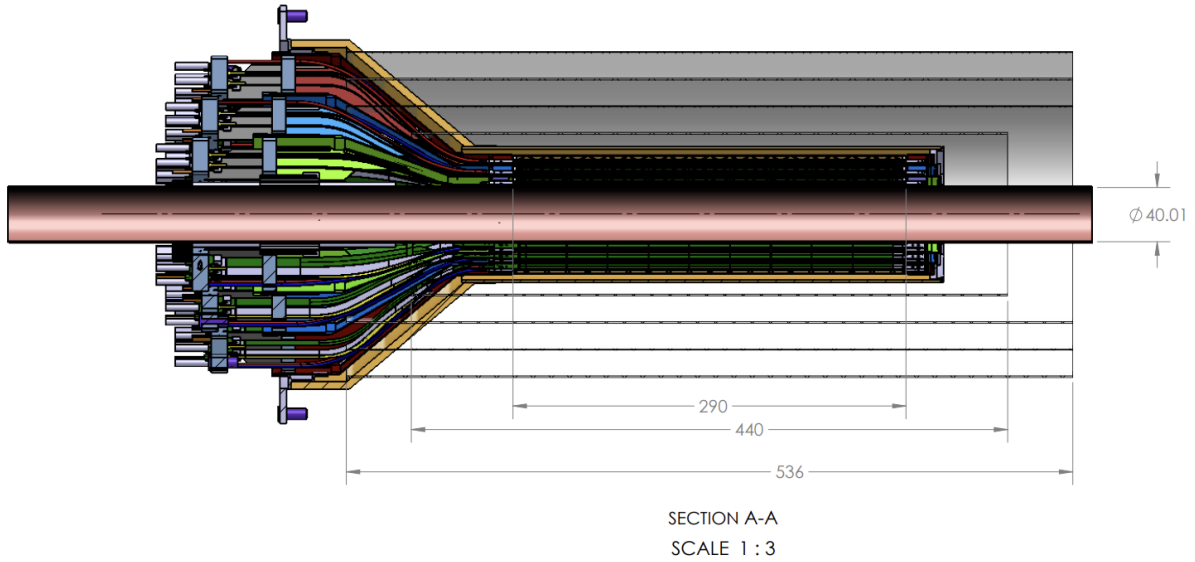
4]. The ALPIDE sensors are Monolithic Active Pixel Sensors (MAPS) that use Complementary Metal Oxide Semiconductor (CMOS) technology to build the pixel directly on the read out chip. The sensor consists of a silicon die of size 15 mm x 30 mm with an active p-doped epitaxial layer where charge is freed by an incoming particle and a set of charge collection diodes (pixels) with position resolution of 30  $\mu\text{m}$  where the charge is then collected. Following collection, the sensors also amplify and digitize signals from each pixel and zero suppression is applied before read out. The MVTX is essential in sPHENIX’s ability to make heavy flavor measurements [5]. By utilizing its high precision position resolution and streaming readout capabilities, the MVTX can reconstruct a large sample of decay vertices from heavy flavor hadrons.

The INTT is a two-layer silicon barrel subsystem located between the MVTX and TPC with the first layer at a radial distance of 7.5 cm and second layer at 10 cm and has full azimuthal coverage, which is ensured by staggering the silicon sensors of the two layers in  $\phi$ . The INTT barrels are composed of silicon ladders containing silicon strip sensors, readout chips, high-density interconnect cables and a carbon fiber stave that serves as a support structure [6]. At the silicon sensor, electron-hole pairs are created when charge particles pass through the detector. This signal is then digitized, zero suppression is applied and the data is read out via the high-density interconnect cables to readout cards. INTT hits can be used to bridge the MVTX and TPC tracks to improve tracking reconstruction. However, the INTT is also essential in associating reconstructed tracks with data from the sPHENIX calorimeter system and global detectors which are readout in triggered mode. This is done by using the precise timing resolution of the INTT hits, therefore reconstructed tracks can be associated with RHIC bunch crossings by using the timing of their INTT hits [6].

The TPC is the main sPHENIX tracking subdetector, spanning in radial distance from 20 to 80 cm with full azimuthal coverage ( $0 < \phi < 2\pi$ ) and pseudorapidity coverage of  $|\eta| < 1.1$ . The sPHENIX TPC is a cylindrical double-sided TPC design with a central membrane at the center of the detector and two readout endcaps on the interior of either side of the detector’s span in z. In each half of the TPC, an electric field is formed by setting the central membrane electrode to



(a) MVTX stave and half-barrel layer



(b) MVTX detector barrel

Figure 2.4: (a) Schematic of an sPHENIX MVTX stave (left) and half barrel layer made up of staves and service section (right). (b) Cross-section of MVTX silicon barrel with its 3 layers highlighted in different colors (Red, Green, and Blue) and sPHENIX beam pipe included to highlight the MVTX location relative to the beam pipe. Reproduced from [3].

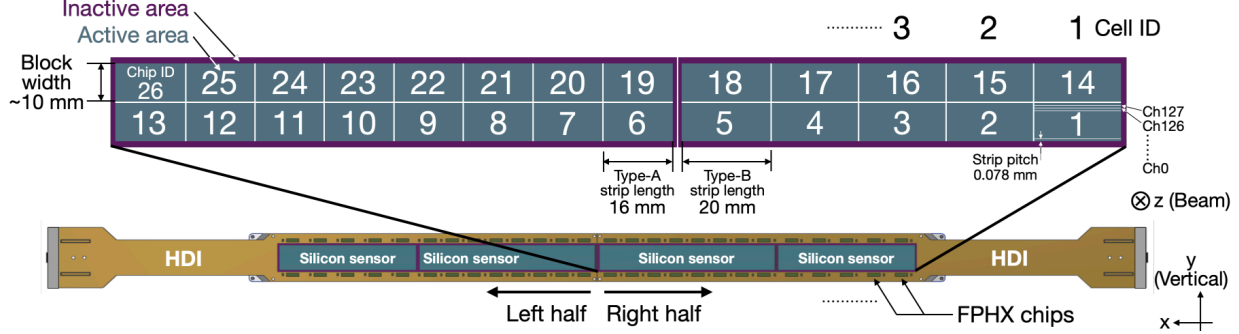


Figure 2.5: Schematic of sPHENIX INTT silicon ladder component. Highlighted on silicon ladder are silicon sensors, readout chips and high-density interconnect (HDI) cables. Reproduced from [6].

a high voltage and the readout endcaps to ground [7, 8]. This electric field is constrained in the radial direction by field cages on the inner and outer cylindrical surfaces of the TPC. The TPC volume is also filled with a gas mixture of Argon, CF<sub>4</sub> and Isobutane in a ratio of 75:20:5. When charged particles from the collision pass through the TPC gas volume, they ionize the gas creating electrons and ions, which act as signal for use in determining particle trajectories through the TPC. These freed electrons then drift towards the readout endcaps via the electric field between the central membrane and the readout endcaps.

On each end of the TPC there is an amplification region where Gaseous Electron Multipliers (GEM) modules are used to amplify the signal from ionized electrons within the TPC volume. Each GEM module contains a stack of four Kapton + Copper foils with a varying voltage across each foil creating a high electric field within the holes of the foils. As electrons pass through the full GEM stack they undergo avalanche amplification, where each foil contributes a small amount of the overall electron amplification. The electric fields between the GEM foils are also able to minimize the amount of avalanche induced positive ions that drift back into the TPC volume thereby reducing ion back flow and allowing the TPC to operate continuous readout. Finally the amplified electron signals are read out using SAMPA chips developed by ALICE each which contain 32 channels. The TPC has a total of 159,744 readout channels read out through a set of 6, 8 and 12 Front End Electronics (FEE) corresponding to the inner (R1), middle (R2) and outer (R3) radial regions of

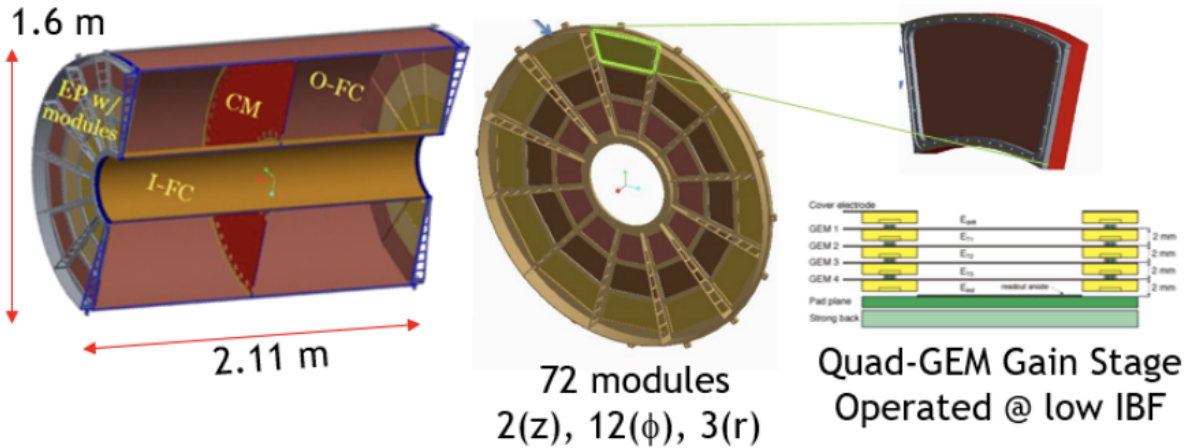


Figure 2.6: Left: Cross-section schematic of sPHENIX TPC showing central membrane (CM), inner- and outer-field cages (I-FC, O-FC) and end plates (EP). Middle: Segmentation of TPC endcap into 72 GEM modules. Right: Schematic of TPC GEM modules highlighting the four foil layers with varying electric fields and pad plane for readout of amplified signal. Reproduced from [7].

the TPC endcaps.

The TPOT is a Micromegas-based detector located just outside the TPC outer cylinder and used for facilitating in-situ TPC calibration by measuring real time distortions in the electron drift within the TPC [9]. The TPOT covers a total of 8% of the TPC acceptance and comprises four modules which cover the full  $z$  range of the bottom-most TPC sector and four addition modules, split between the two neighboring TPC sectors in  $\phi$ . Each module contains two radially stacked Micromegas chambers where the first chamber measures the  $z$  coordinate and the second measures the  $\phi$  coordinate of a transversing particle. Each Micromegas chamber contains a drift electrode, a micromesh, a resistive layer and a readout layer with an electric field applied across the layers to guide ionization electrons through the drift gap. The micromesh separates the ionization electron drift and amplification regions and the readout layer collects signals which are then read out via a set of front end electronics (FEEs).

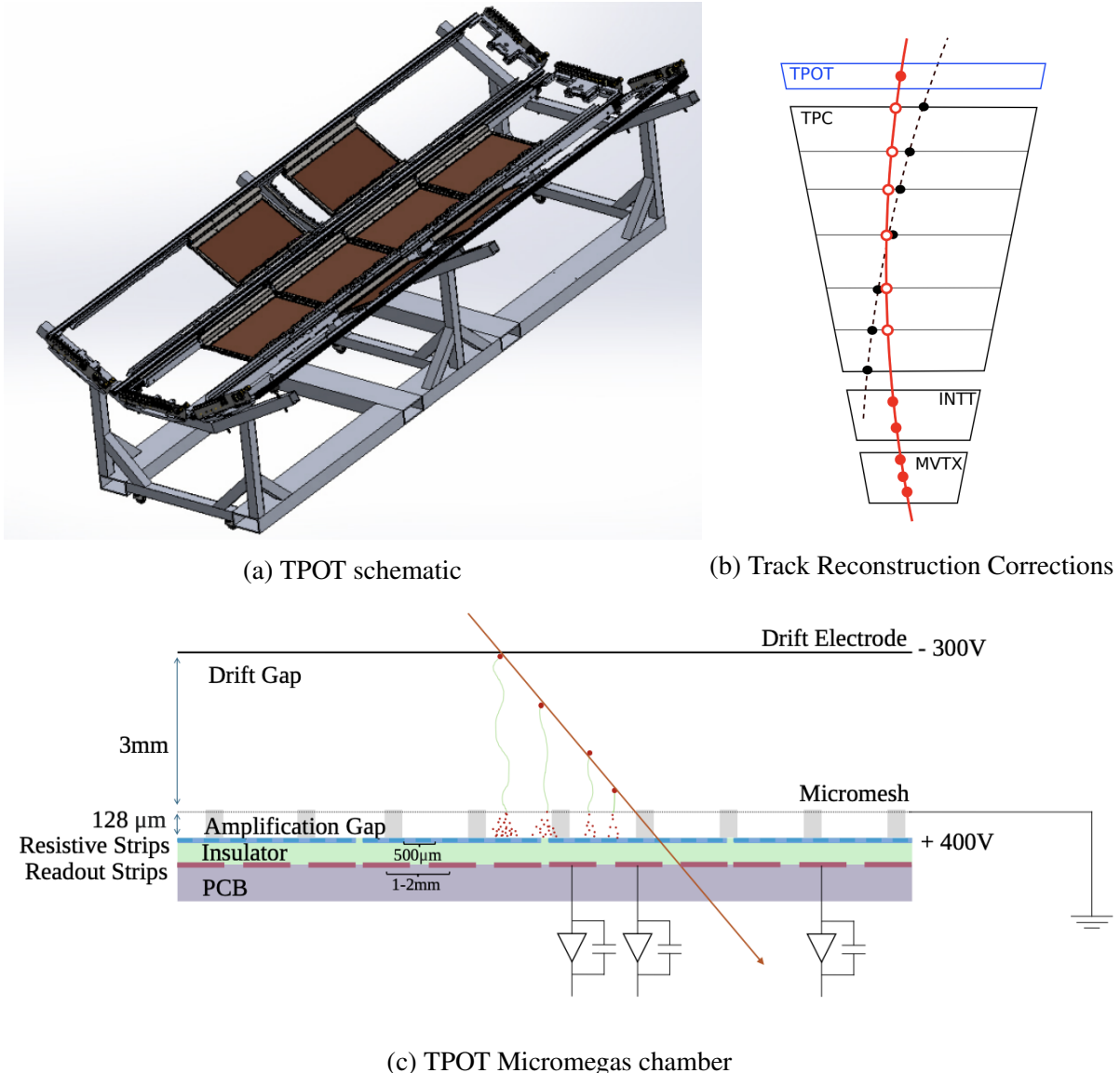
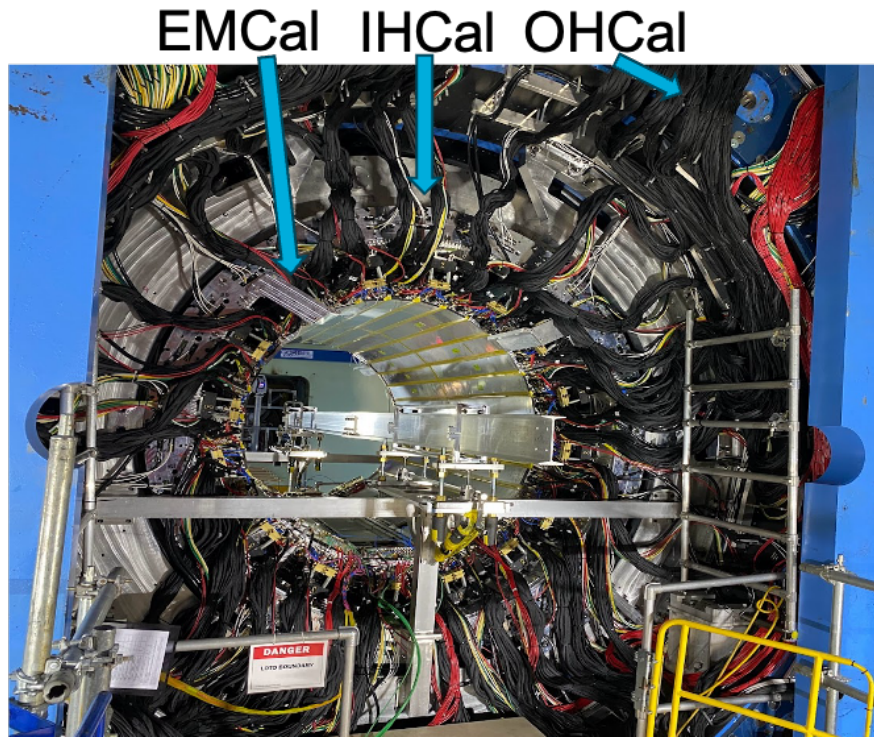


Figure 2.7: (a) Schematic of sPHENIX TPOT detector (left). (b) Schematic of track reconstruction using all tracking subsystems highlighting the benefit to having a TPOT hit for drift corrections. (c) Cross-section of TPOT Micromegas chamber. Reproduced from [9].

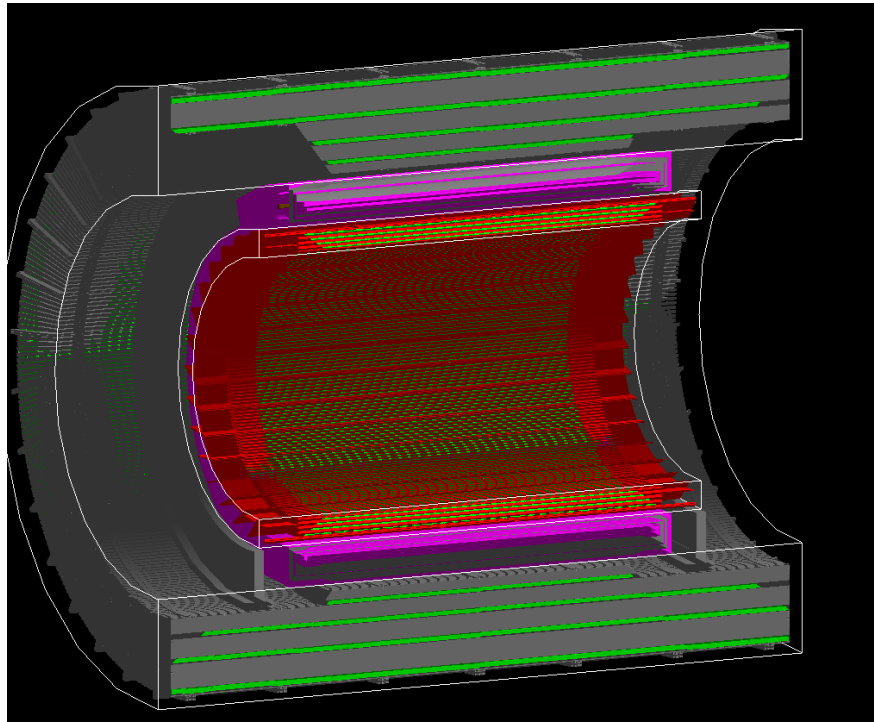
## 2.2.2 sPHENIX Calorimeter System

sPHENIX has three central barrel calorimeter layers, an electromagnetic calorimeter (EMCal), an inner hadronic calorimeter (IHCal) and an outer hadronic calorimeter (OHCAL). These calorimeter subdetectors provide energy measurements of all particles, both neutral and charged, for use online in triggering on rare physics probes like high momentum photons and jets and offline for use mainly in jet measurements. These detectors are concentric and sandwich the sPHENIX magnet with the EMCal located closest to the interaction point and the OHCAL located further from the interaction point within the calorimeter system. Further, these detectors have full azimuthal coverage ( $0 < \phi < 2\pi$ ) and pseudorapidity coverage of  $|\eta| < 1.1$ .

The sPHENIX EMCal is designed to precisely measure photons, electrons and positrons via electromagnetic showers. To achieve this goal, the EMCal has a depth of 18 radiation lengths and its electromagnetic shower resolution was measured in beam tests to be  $2.8\% \oplus 15.5\%/\sqrt{E}$  for electrons [10, 11]. The EMCal is also nearly one nuclear interaction length in depth and therefore sees a substantial amount of energy in the ion collisions from hadronic showers as well. The sPHENIX EMCal is a compact sampling calorimeter; it is located just outside of the TPC/TPOT with an inner radius of 90 cm and the EMCal and IHCal combined are constrained to fit within the repurposed Babar magnet. The EMCal uses a tungsten powder absorber, which has a small Moliere radius and large particle stopping power. This allows the EMCal to have a large number of radiation lengths and precise position resolution while still being compact. Scintillating fibers embedded within the tungsten powder collect and transmit light to a lightguide on the front of each EMCal block (size 2x2 towers). Following collection by the lightguide, the signals are processed by Silicon Photomultipliers (SiPMs), which convert the light to electric current, and are passed through a pre-amplifier. The analog voltage signals are then passed to the Analog-Digital Converters as the start of the sPHENIX calorimeter data acquisition system. The EMCal is composed of 64 sectors, 2 sectors in  $\eta$  and 32 sectors in  $\phi$ , with each sector containing 384 towers for a total of 24,576 EMCal towers of tower size  $\Delta\eta \times \Delta\phi = 0.024 \times 0.024$ . Each sector has six interface boards used to communicate with the detector for setting and monitoring the detector state, including information

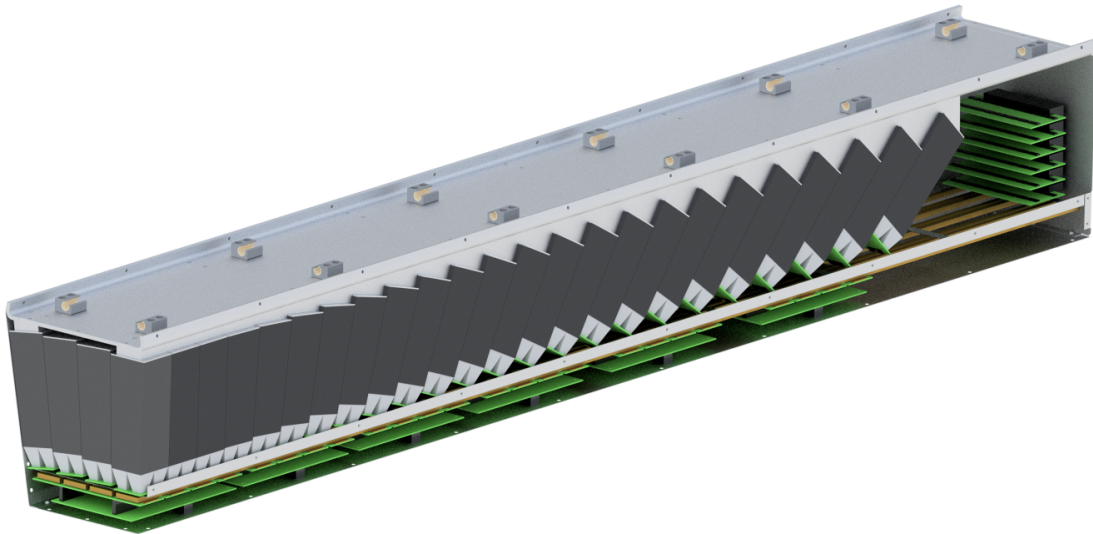


(a) Installed EMCal, IHCAL and OHCal

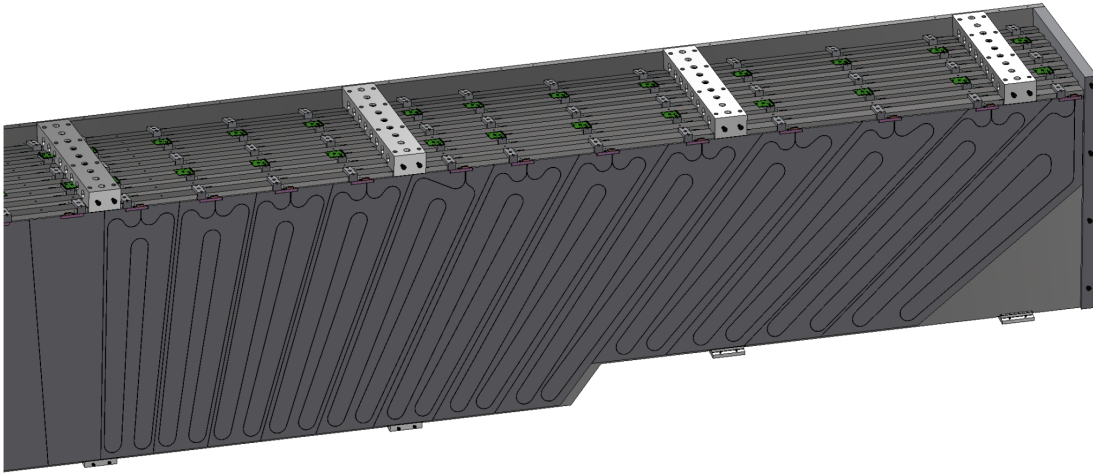


(b) IHCAL, Magnet, OHCal Simulated Graphic

Figure 2.8: (a) Photo of the sPHENIX EMCal, IHCAL and OHCal detectors after installation and cabling. (b) Graphic of sPHENIX IHCAL (red), OHCal (gray) and superconducting magnet (pink) from GEANT simulation. IHCAL(OHCal) scintillator tiles shown in yellow(green).



(a) EMCal Sector Schematic



(b) OHCal Sector Schematic

Figure 2.9: (a) Schematic of EMCal sector highlighting projective geometry of towers in  $\eta$  and lightguides and electronics on the inner radius of the sector. (b) Schematic of OHCal half-sector highlighting projective geometry of towers in  $\eta$ , layered absorber/scintillator tile tower design, wavelength-shifting fiber located within HCal scintillating tiles, and readout electronics on the outer radius of the sector. Reproduced from [7].

about the SiPM temperatures, bias voltage and offsets supplied to the SiPMs, leakage current, and detector gain. These slow control communication boards are also used for detector commissioning tasks such as turning on and pulsing LED and test pulses for calibration runs.

The sPHENIX HCal system is the first central barrel hadronic calorimeter on a detector at RHIC and allows for full jet reconstruction with both electromagnetic and hadronic calorimetry at RHIC energies for the first time. sPHENIX is designed to measure hadronic showers with the full calorimeter system totaling a depth of 5 nuclear interaction lengths and having a hadron resolution response in beam tests of  $13.5\% \oplus 64.9\%/\sqrt{E}$  [11]. The HCal system is split into two layers, the IHCAL and OHCal, separated by the Babar superconducting magnet repurposed for sPHENIX. The IHCAL is located between the EMCal and the magnet with an inner radius of 117 cm and outer radius of 134 cm and the OHCal is located outside of the magnet acting as the magnet flux return with an inner radius of 183 cm and an outer radius of 269 cm. The IHCAL (OHCal) are sampling calorimeters composed of alumininum (steel) aborber plates and 4 (5) scintillating tiles set at an angle offset to the transverse direction to reduce the amount of collision particles that do not interact with the active volumes of these calorimeters. Wavelength shifting fibers are embedded within the scintillating tiles which collect and transmit the produced light to SiPMs. The SiPMs process this light into voltage signals which is then amplified and digitized in the same manner as for the EMCal. Both the IHCAL and OHCal contain 32 sectors split into North and South half-sector sides and each sector contains 48 towers for a total of 1536 towers of tower size  $\Delta\eta \times \Delta\phi = 0.01 \times 0.01$ . Each half sector has one interface and slow control communication board and these are also used to set and monitor the detector state including SiPM temperatures, bias voltages and offsets, leakage current and detector gain.

### 2.2.3 sPHENIX Global Detectors

sPHENIX contains several global detectors used to provide minimum bias event triggering and total event characterization information such as the vertex of the collision event and centrality of the event. These detectors include the Minimum Bias Detector (MBD), Zero Degree Calorime-



Figure 2.10: Left: Schematic of 64 MBD module array mounted on detector frame. Right: Photo of individual MBD module with quartz radiator and PMT. Reproduced from [7].

ters (ZDCs) and sPHENIX Event Plane Detector (sEPD).

The MBD is located at forward rapidity,  $3.51 < |\eta| < 4.61$ , on both the north and south side of the interaction point, close to the beam pipe, and is repurposed from the PHENIX Beam Beam Counter (BBC) with updated trigger and readout electronics, where it was located in a different position  $3.0 < |\eta| < 3.9$  along the beam line [12, 13]. Each side of the MBD contains a set of 64 1-in diameter mesh-dynode photomultiplier tubes (PMT) and the front of these PMTs are connected with a 3 cm quartz Cherenkov radiator to detect charged particles via Cherenkov radiation. During both PHENIX and sPHENIX running, the MBD has been located close to the beam pipe and is subject to high levels of radiation during data taking. In its original design, quartz was selected for the radiator material and PMTs for signal amplification due to their radiation hardness and over the data taking lifetime of the MBD, the subsystem has not seen any significant degradation due to radiation damage. The MBD is used for online triggering of hadronic interactions and offline to provide a selection of minimum-bias (MB) events and centrality determination in heavy-ion collisions. It is also used for the offline reconstruction of the collision z-vertex position using the arrival time difference between the first charged particles detected by the PMTs on the north and south side of the interaction point.

The ZDCs [14] are located on both sides of the interaction point at very forward rapidity, 18 m

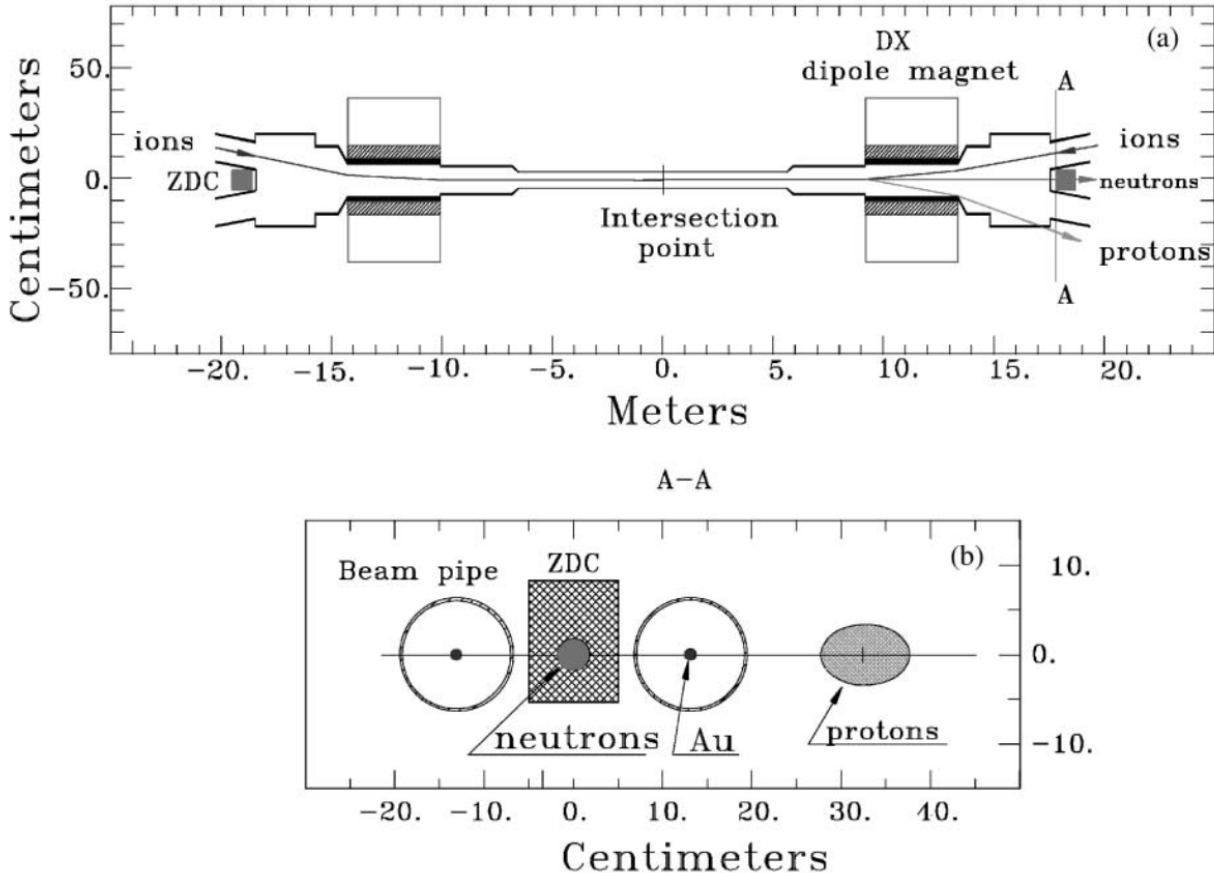


Figure 2.11: Schematic of sPHENIX ZDC detector shown from (a) collision region view and (b) "beam's eye" view to show the ZDC location past the RHIC DX dipole magnets and between the beam pipes. Also shown is the trajectory of beam fragments with neutrons measured in the region of the ZDC and protons deflected. Reproduced from [14].

from the interaction point, and are also repurposed from the PHENIX detector. They are sampling hadronic calorimeters composed of three modules made of tungsten alloy and PMMA optical fiber with a total of 5.1 nuclear interaction lengths (149 radiation lengths). Utilizing their very forward location, the ZDCs are able to detect beam fragment neutrons of the collision without additional backgrounds from produced particles and secondaries from the collision. A schematic showing how the sPHENIX ZDC detector measures these beam fragment neutrons while not being sensitive to beam fragment charged particles can be found in Fig. 2.11. The total energy of the neutrons are measured in the ZDCs via the transmission of Cherenkov radiation from the neutron's hadronic showers by PMMA fibers to PMTs. Each side of the ZDC is calibrated by requiring that the peak in

the measured energy distribution which corresponds to the energy deposition of a single neutron is set at the nominal beam energy value of 100 GeV. Additionally, specifically in sPHENIX, criteria on signals in both sides of the ZDC are included in the minimum bias event selection to separate hadronic interactions from beam backgrounds like beam-gas interactions.

#### 2.2.4 sPHENIX Data Acquisition and Readout

sPHENIX is designed with a state of the art data acquisition system and computing resources to collect data at very high rates which is necessary to achieve its data-intensive physics goals within its short three year running period. The sPHENIX data acquisition system is designed to readout data from triggered calorimeter events at a rate of 15 kHz in both  $p+p$  and Au+Au collisions and read out tracking detectors in full streaming mode collecting all of the supplied collision data. With the high collision rate ( $\gg 15$  kHz) supplied by RHIC, the sPHENIX trigger system is used to make decisions using information from the calorimeter and global detectors on whether to read out a particular collision event. This trigger system uses calorimeter information to identify and save likely high  $p_T$  photon and jet events and uses the global detectors to identify and save minimum bias hadronic collision events.

The triggered calorimeter and global detector data is read out passing through five steps: first the front end modules (FEM) digitize the analog signals from the SiPMs and PMTs in the detectors, second the data collection modules (DCMs) combine data from multiple FEMs and act as very short term buffers. The data is then passed through the sub event buffer (SEB) computers used to store the data temporarily, and then is transferred to bufferboxes, before finally being written to disk storage. The tracking data is read out from the front end electronics (FEEs) through the ATLAS "FELIX" card which is connected directly to a standard computer which serves as a buffer similar to the triggered SEBs. The tracking data is also transferred to bufferboxes and written to disk storage in the same manner as the triggered data.

The Really Cool Data Acquisition (RCDAQ) system is used to control and coordinate the entire sPHENIX data acquisition and readout process. The RCDAQ coordinates the start and stop of all

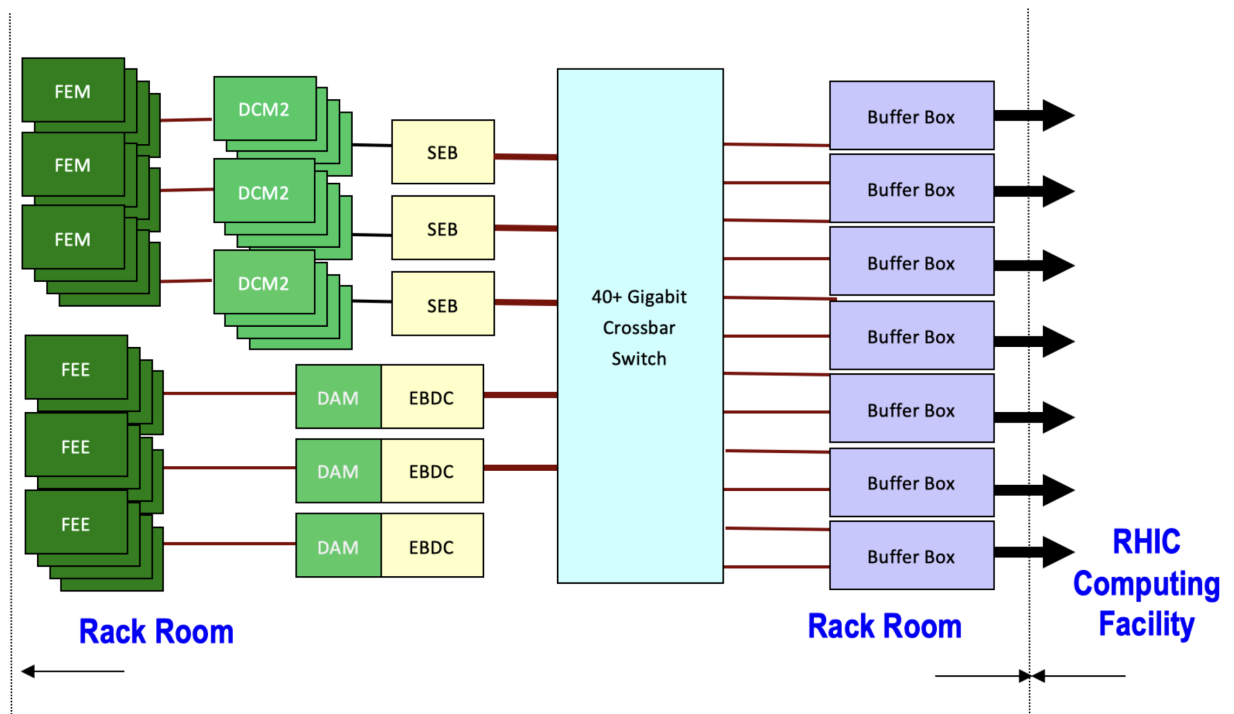


Figure 2.12: Flowchart of sPHENIX data acquisition system showing propagation through the stages of data acquisition from the front end electronics to the RHIC computing facility. Reproduced from [7].

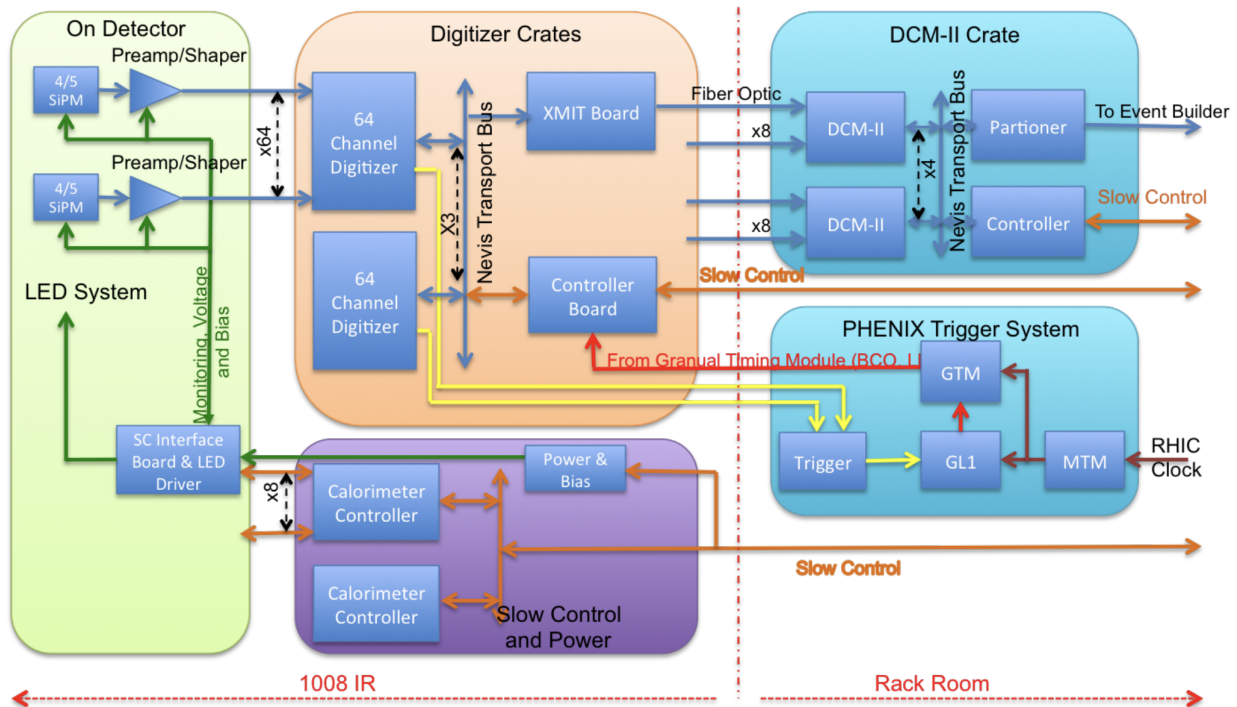


Figure 2.13: Detailed flowchart of sPHENIX data aquisition system for triggered subsystems (calorimeters and global detectors) including feedback on data readout from Trigger System. Reproduced from [7].

of sPHENIX's independent read out data streams and transmission of data of variable types with fixed packet sizes through the different stages of buffer computers. This is necessary to ensure that all subsystems are synchronized in their read out and is especially important since in sPHENIX all subsystem components have independent data stream read out and there is no online event building. Via the transmission of data packets with fixed sizes, the RCDAQ is also able develop a controlled and steady flow for the data through the read out system.

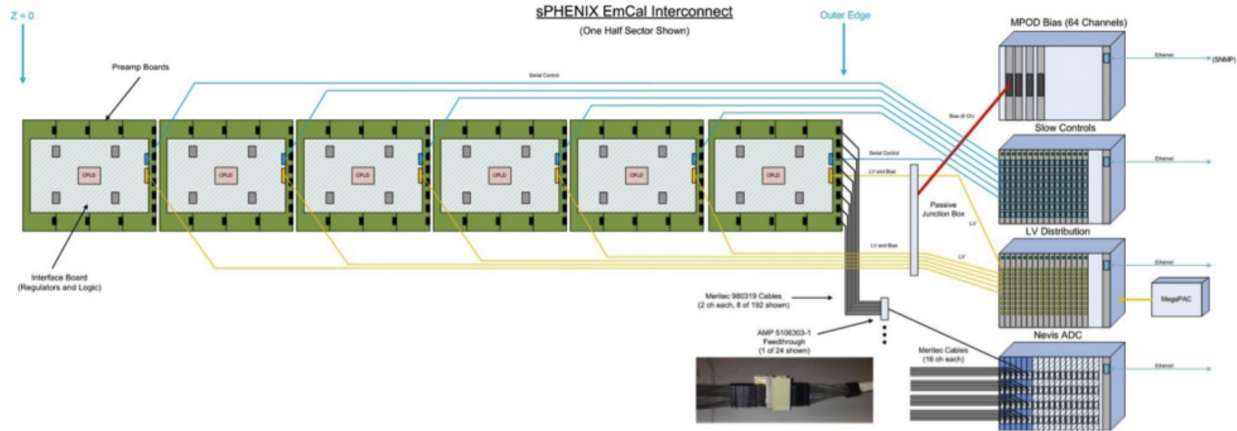
## **Chapter 3: sPHENIX Calorimeter Commissioning, Reconstruction and Calibration**

Substantial work on the calorimeter commissioning, reconstruction, and calibration was necessary before producing high-quality physics results using the sPHENIX calorimeters. This commissioning work included devising and implementing real-time monitoring and logging of the calorimeter detector state and investigating various reconstruction issues in the calorimeter data related to read out electronics issues. Additionally, a vast array of calorimeter calibrations were also necessary to accurately reconstruction the correct energy scale of the calorimeter signals.

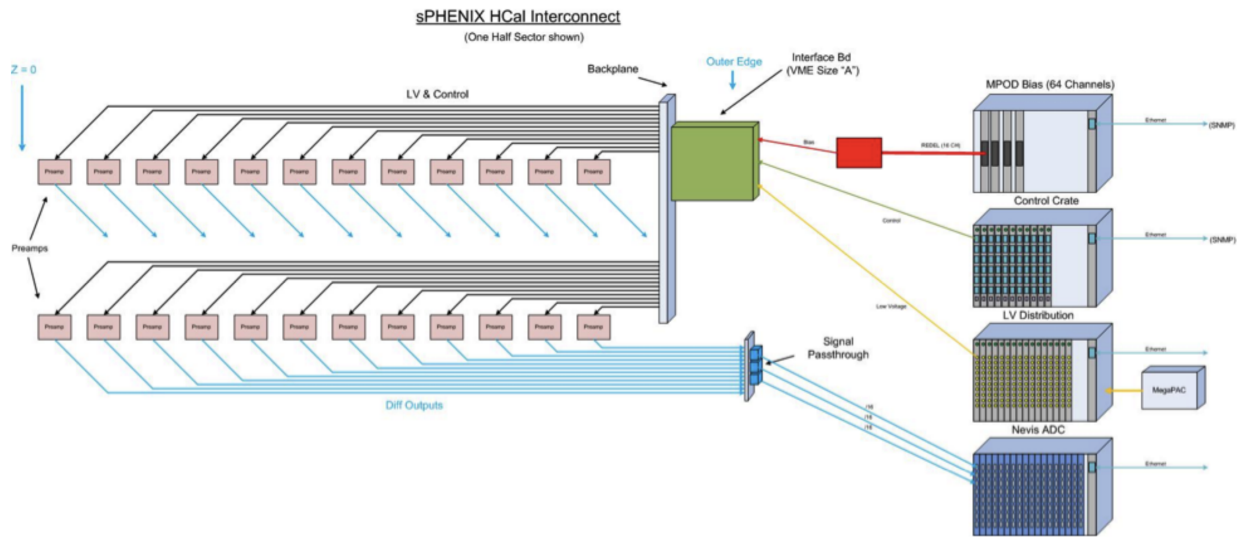
### **3.1 Real-time Calorimeter State Logging and Monitoring**

Each EMCal sector has six interface boards used to communicate with the detector for setting and monitoring the detector state. Each interface board is connected to a slow control communication board, a Multi-channel Power Output Device (MPOD), a low voltage power supply, and an Analog-to-Digital Converter (ADC) board. The slow control communication board is used to set the detector state including information about the SiPM temperatures, set value for the low and bias voltage, tower by tower bias voltage offsets supplied to the SiPMs, tower by tower leakage current from the SiPMs, and pre-amplifier gain mode. These slow control communication boards are also used for detector commissioning tasks such as turning on and pulsing LED and test pulses for calibration runs. A similar control scheme is used for communication with the IHCAL and OHCAL. Here each IHCAL and OHCAL half sector has one interface and slow control communication board and these are also used to set and monitor the detector state including SiPM temperatures, bias voltages and offsets, leakage current and pre-amplifier gain mode.

This information about the detector state is vital both during the online operation of the detector



(a) EMCal Sector Communication Design



(b) IHCAL/OHCAL Half-Sector Communication Design

Figure 3.1: (a) Diagram of EMCal sector design with interface board connections to slow control, MPOD, low voltage power and ADC boards. (b) Diagram of HCal half-sector design with interface board connections to slow control, MPOD, low voltage power and ADC boards. Reproduced from [7].

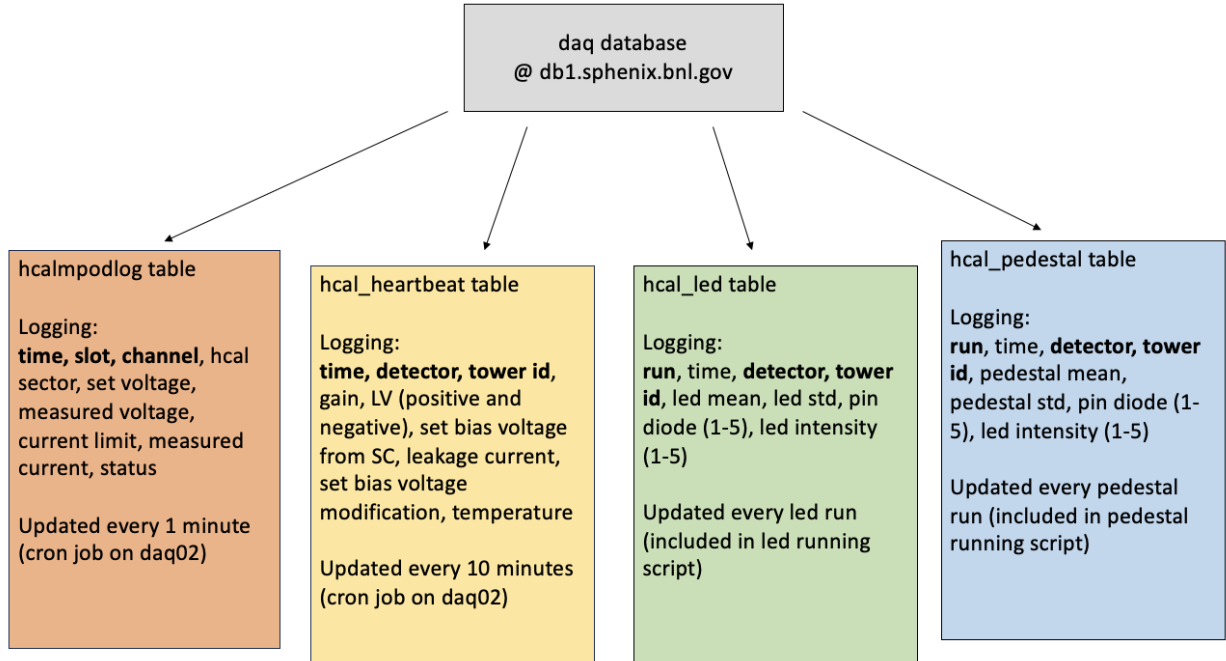
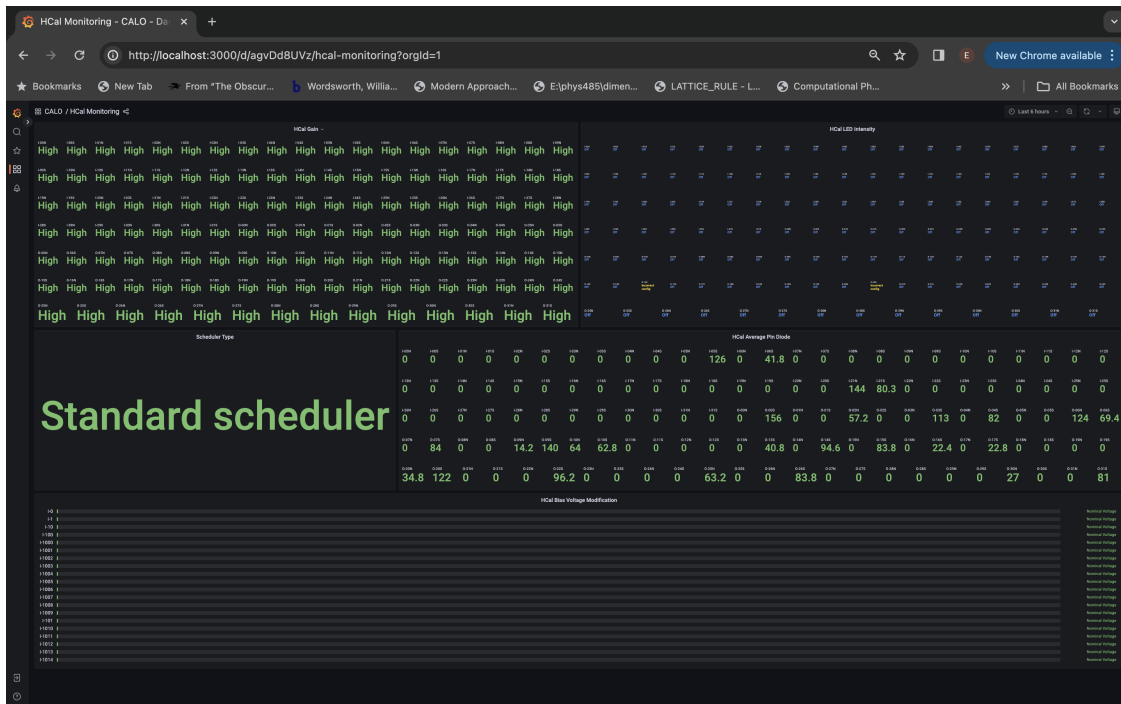


Figure 3.2: Diagram of HCal database table schema for logging detector state information. Includes tables for hcal slow control and bias voltage information as well as LED and pedestal run analysis results.

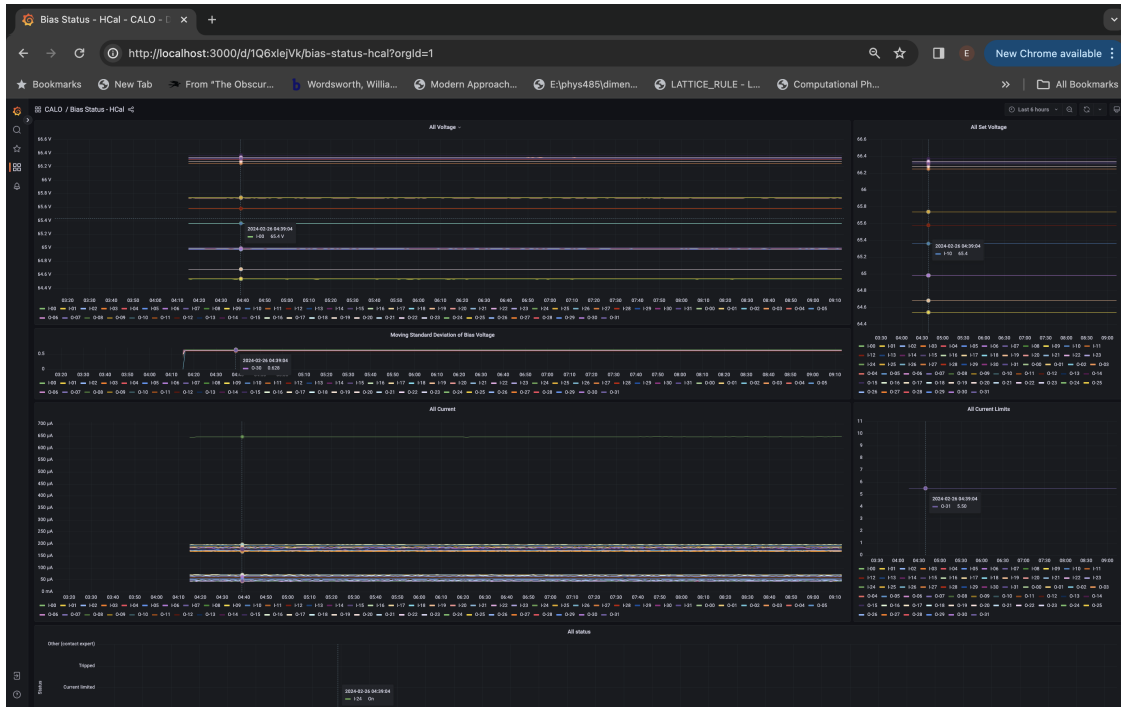
and during offline reconstruction and calibration of the data. The detector state information for both the EMCAL and HCal is logged in real time by first communicating with the slow control communication boards via a telnet connection, parsing the response, and then writing the detector state information to a PostgreSQL database. The detector state information has been logged up to every 10 minutes for the last three years of data taking.

To accurately map the detector state information into a useable format for reconstruction and calibration, the detector information is keyed on the offline tower id and timestamp of the log entry. This allows for easy access to the tower by tower information for use in calibration tasks such as applying corrections to the HCal absolute energy calibration due to changes in SiPM operating temperature over periods of data taking.

The detector state information is also used to monitor the well-being of the detector in real time. Grafana dashboards, which provide an aggregate view of the logged detector state information, are used by data taking shifters to monitor well-being of the detector in real time. In order to present



#### (a) Shifter Monitoring Dashboard



### (b) Bias Voltage Monitoring Dashboard

Figure 3.3: (a) Shifter monitoring dashboard for HCal gain, SiPM temperature and bias voltage offsets, LED and Pin Diode status. (b) Bias voltage monitoring dashboard showing the bias voltage for sector of the HCal.

clear descriptions of the detector state, the tower by tower information stored in the database is queried and then aggregated to present the overall health of individual sectors or half-sectors of the calorimeters. These dashboards include both real time and time series information on the SiPM and pre-amplifier temperatures, the bias voltages, whether the tower by tower bias voltage offsets are set to their nominal values, and gain modes.

## 3.2 sPHENIX Low-Level Data Reconstruction

During the first year of data-taking, the sPHENIX calorimeters collected a commissioning dataset of Au+Au collision events. These events were used to exercise the data production, reconstruction, and calibration chains. Hot towers found in this commissioning dataset due to issues with the digitization were studied and a set of characteristic failure modes in the digitization and read out process were determined.

### 3.2.1 Diagnosing ADC Bit Issues

The calorimeter digitization and read out is performed via digitizer boards originally designed for PHENIX [7]. These digitizer boards first read in differential analog signals from a total of 64 channels. The Analog Device AD9257 on the boards perform a digitization of each analog signal to 14-bit digital precision operating at 6x the Beam Crossing Clock (17.6 ns). The serialized data from the ADC chip is then received by the ALTERA Arria V GX FPGA on the boards which triggers optical read out of the digitized signal information. A diagram of the ADC board design is shown in Figure 3.4.

Two main cases of abnormal behavior for calorimeter waveforms were found in the Run 2023 commissioning dataset. The first case of abnormal waveform shape was characterized by waveforms with gaps of ADC counts in  $2^n$  and this behavior was found to persist in every event for a channel across an entire run. The second case was characterized by waveforms with stuck bit or "bit flip" for a time sample in the digitized waveform and was found to occur intermittantly throughout a run.

### sPHENIX ADC Module Block Diagram

RHIC beam clock 9.6MHz

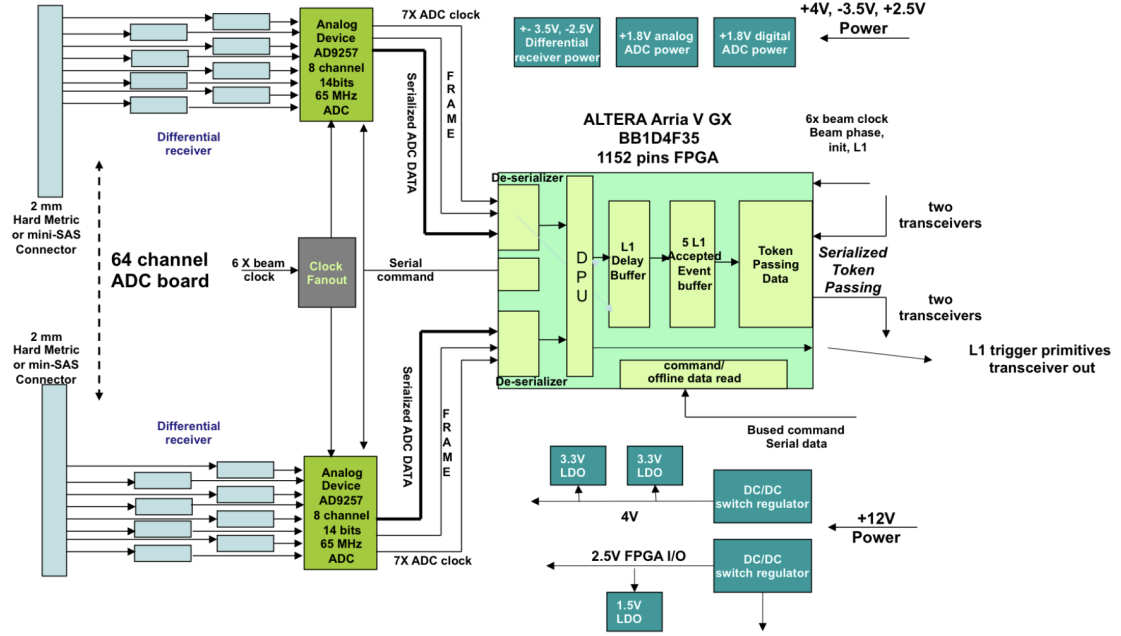


Figure 3.4: Diagram of the ADC board design used for digitization of signals from the sPHENIX calorimeters. Reproduced from [7].

### 3.2.2 Online ADC Firmware Fixes

For the first case of abnormal waveforms where the waveforms always exhibited a gap of  $2^n$  between digitized waveform values for particular time samples the binary sequence of the waveform values was studied in detail. The values of  $n$  were found to be constant for a given channel over an entire run and could be any value between 1 and 13. After studying the binary sequence of the waveform values, it was found that the digitized waveform value in binary (the 14-bit bit-stream) was being shifted by a number of bits related to the number  $n$  in the  $2^n$  gaps. An illustration of this shift in the read out bit-stream and examples of these shifted bit-stream waveforms and resulting waveforms from un-shifting these bit-streams is shown in Figure 3.6.

The ADC configuration procedure was intended to use a fake-data test sequence available locally on the ADC to test that the bit alignment is correctly set. However, the configuration procedure was missing the validation step of the test sequence alignment. Therefore in cases when the bit alignment step of the ADC configuration procedure failed, no error was thrown in the configu-

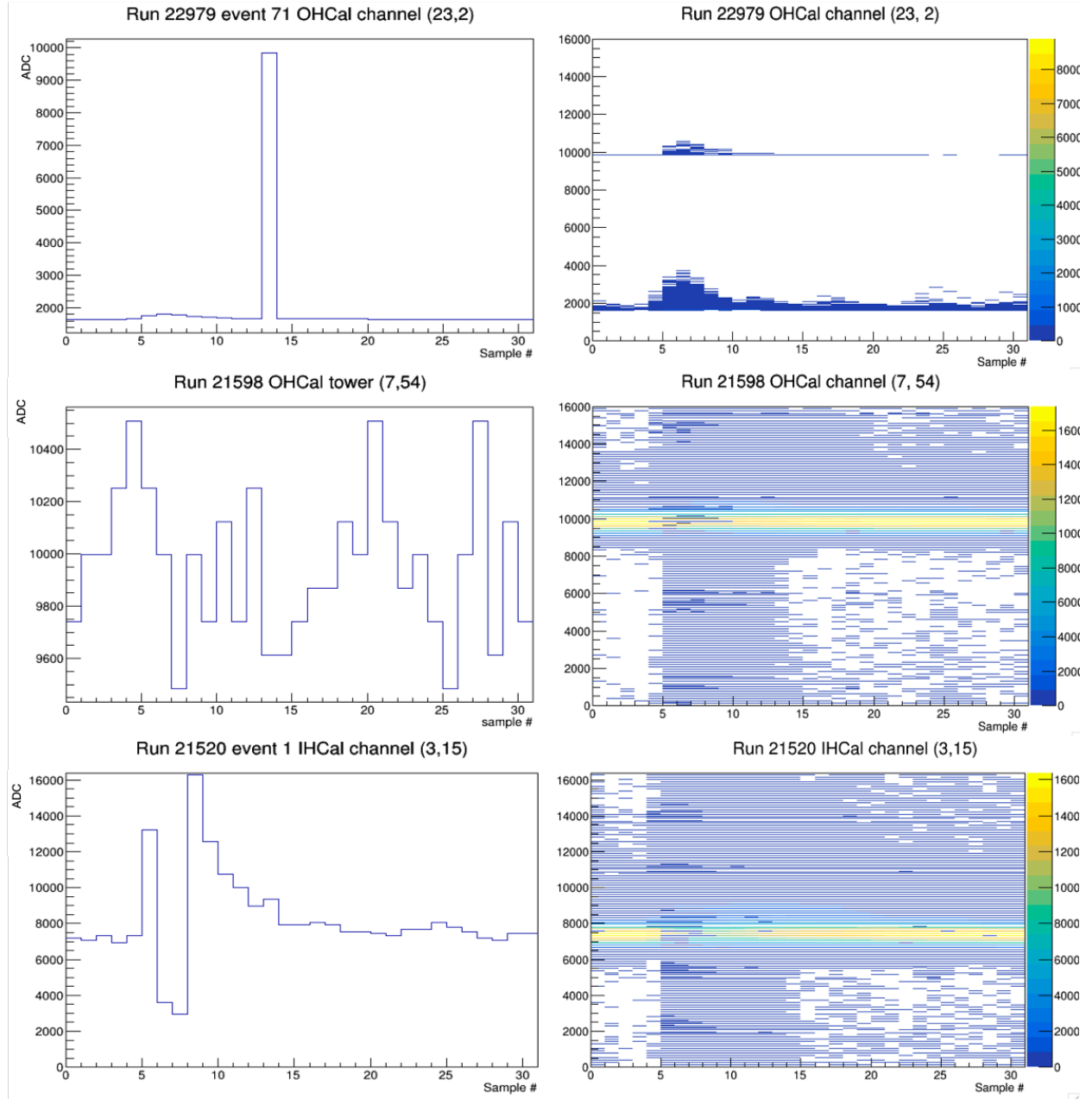


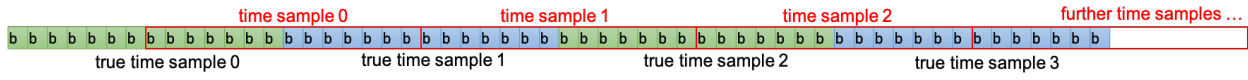
Figure 3.5: Examples of abnormal waveforms with bit flip (top) or  $2^n$  gaps of ADC counts (middle and bottom) behavior. Left plots show the abnormal waveforms for a single event. Right plot show a peristancy plot of the channels waveforms overlaid for an entire run.

ration sequence and mis-aligned ADCs were reading out data for full runs. This led to a situation where the ADCs were mis-aligned by any number of bits and the read out waveforms had gaps of  $2^n$  between waveform values for particular time samples. To solve this issue, a step was added to the ADC configuration procedure to validate the bit alignment step using the fake-data test sequence and rerun the alignment in the case that the fake-data alignment test does not pass. This fix was implemented into the online ADC configuration procedure and this abnormal waveform issue was resolved for all calorimeter channels.

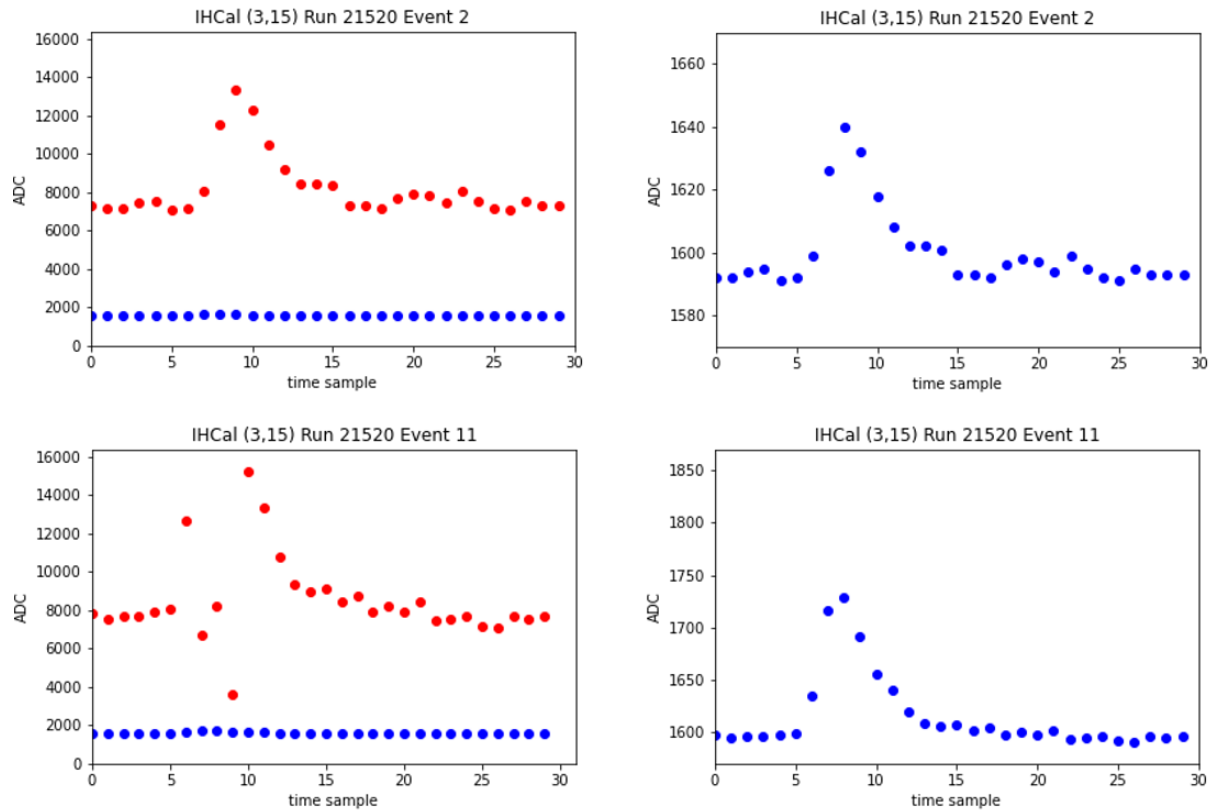
### 3.2.3 Offline Reconstruction Software Fixes

A small fraction (<0.1%) of the ADC channels in the sPHENIX calorimeters were determined to have intermittent stuck bits due to hardware issues with the ADCs. For these ADC channels with known stuck bit phenomena, around 1% of events in a run will have a waveform with a stuck bit. In the default calorimeter reconstruction chain, waveforms from channels with stuck bit issues were masked as energy contributions from towers with high value stuck bits can easily pollute a physics measurement especially studies of rare high-energy jet and photon measurements. This masking was determined by fitting the waveform to a template and masking based on the value of a quality parameter defined as the least squared error over the number of degrees of freedom of the fit. In this default reconstruction chain, waveforms with stuck bit issues have a characteristic high quality parameter (denoted as  $\chi^2$ ) of 10 times the nominal value range.

While this masking was effective, in an effort to maximize calorimeter acceptance and minimize event-by-event changes in the calorimeter acceptance, a recovery scheme at the offline waveform fitting stage was devised to "un-flip" the stuck bits and recover a high quality, useable waveform. The goal of this recovery method was fairly constrained as to not introduce any reconstruction artifacts into the calorimeter reconstruction chain. Therefore, the recovery method focused on a set of abnormal waveforms where the underlying waveform shape was well understood and the recovery procedure was easy to validate and replicate. The constrained goal was to recover as many single sample bit flip waveforms as possible from waveforms with characteristic high value



(a) Diagram of shifted bit-stream read out for single ADC channel.



(b) Examples of shifted bit-stream waveforms and recovered waveform after re-shifting bit-stream.

Figure 3.6: (a) Diagram of shifted bit-stream read out for a single ADC channel in the case of misalignment during ADC configuration step. (b) Examples of abnormal shifted bit-stream waveforms in red and waveforms after re-shifted recovery procedure in blue. Right figures included to show re-shifted waveforms in detail.

```

if (chi2min > _chi2threshold && f->GetParameter(2) < _bfr_highpedestalthreshold && _dobitfliprecovery) {
    std::vector<float> rv;
    for (int i = 0; i < size1; i++) {
        rv.push_back(v.at(i));
    }
    int bits[3] = {8192,4096,2048};
    for (int b = 0; b < 3; b++) {
        for (int i = 0; i < size1; i++) {
            if ((int(rv.at(i)) % bits[b] != int(rv.at(i)) && int(rv.at(i)) % bits[b] > _bfr_lowpedestalthreshold) {
                rv.at(i) = rv.at(i) - bits[b];
            }
        }
    }
    /* rerun template fit method */
    if (recover_chi2min < _chi2lowthreshold) { } Check if new fit chi2 is good using same chi2 threshold as isBadChi2 status
    /* replace waveform with temporary waveform and push new fit parameters + recovered status back to TowerBuilder */
} else {
    /* use original waveform and old fit parameters + not recovered status back to TowerBuilder */
}
}

```

Create temporary waveform vector for recovery

Iterate through bits  $2^{11}$ - $2^{13}$  and each time sample of the waveform

Check if ADC is above high bit value as well as if subtracting this high bit value would give a value greater than pedestal value, if so do bit subtraction

Check if new fit chi2 is good using same chi2 threshold as isBadChi2 status

Figure 3.7: Pseudo-code algorithm for discovering and recovering calorimeter waveforms digitized with stuck high value bits using the quality of fit to the calorimeter waveform template.

(bits  $2^{11}$  to  $2^{13}$ ) stuck bit behavior which have been previously successfully identified using high  $\chi^2$  signature from the template fit. Within this goal was also to reject performing this recovery procedure on other sources of failure that could cause poor waveform fit quality include channels with the previously mentioned shifted bit-stream, waveforms with abnormal shape, and waveforms with lower value stuck bits (bits  $2^{10}$  and below).

The recovery method is defined below and described using pseduocode in Figure 3.7. First, possible stuck bit waveform candidates are identified using the fit quality ( $\chi^2$ ) and pedestal values return from the waveform's fit to the default calorimeter template. Next, a recovery step is performed on these waveform candidates by iterating through bits  $2^{11}$  to  $2^{13}$  and subtracting this bit value if the waveform sample value is greater than the bit value and the subtracted value is greater than the waveform pedestal value. Following this bit subtraction, the waveform is refit to the calorimeter template and the quality of the fit is re-evaluated. A example of successful execution of this recovery method for a stuck bit  $2^{11}$  is shown in Figure 3.8.

Channels with shifted bit streams are eliminated from the recovery procedure by requiring that the pedestal calculated from the first round of template fit be  $< 4000$  ADC; these shifted bit stream waveforms have pedestals between 8000 and 10000 ADC while range of normal calorimeter

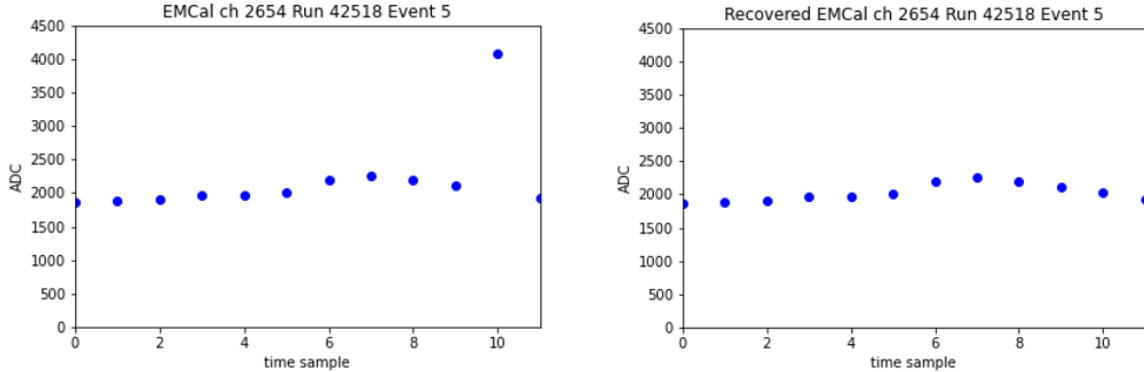


Figure 3.8: Example waveforms of before (left) and after (right) the waveform recovery method for an EMCal channel with a known intermittent stuck bit  $2^{11}$ .

pedestal values are between 1300 and 2000 ADC. Further, channels with very noisy behavior or lower value stuck bits are eliminated from the recovery procedure by requiring that the bit subtraction return a value above pedestal values and the recovered waveform have a good fit quality passing the default fit quality criteria.

### 3.3 sPHENIX Calorimeter Calibration and Reconstruction Routines

#### 3.3.1 Calorimeter Tower Reconstruction

The digitized waveform signals from the calorimeters are reconstructed into energy deposits using a fit to a custom waveform template method which extracts the ADC signal amplitude from each tower in each event. Additionally, tower-by-tower hardware zero suppression (ZS) thresholds set at  $2\sigma$  of the calorimeter pedestal noise were implemented to reduce data volume. Calorimeter tower waveforms with recorded pre-minus-post values below the hardware level ZS threshold only recorded the pre and post samples of the waveform and pre-minus-post values above the ZS threshold recorded the full 12 time sample waveform. During the fitting step of the calorimeter tower reconstruction, an additional software level ZS threshold is applied to correct for biases in the calorimeter energy distribution from noise waveforms. This ZS threshold is higher than the hardware level threshold and uniform across the full detector; for calorimeter tower waveforms which fall below this software level ZS threshold, the pre and post sample values of the waveform

are used instead of fitting the waveform using the template fit method. For the Au+Au ( $p+p$ ) analyses, the software level ZS thresholds were set to 100 (60) ADC for the EMCAL and 50 (30) ADC for each of the HCals.

Both EMCAL and HCal waveform templates were created using beam data from early runs of Run 2024. The template fit has three free parameters: the pedestal, peak time and scale of the waveform, and the processing procedure returns these parameters plus the  $\chi^2$  term representing fit's least-squares over number of degrees of freedom value which acts as a goodness of fit metric. Finally, the calorimeter reconstruction pipeline also includes masking bad towers within the run bad tower masks. A tower is considered hot on a run by run basis, one way for a tower to be considered hot is if the 1% of events with energy above a threshold have a high  $\chi^2$  value for the template fit. Less than 1% of events have a tower in any of the calorimeter layers with a high  $\chi^2$  value that is not already included in the run-by-run bad tower mask. A systematic study of the effect of masking these intermittently high  $\chi^2$  towers on the upcoming measurements found that the effect of masking these intermittently high  $\chi^2$  towers on the event by event level had negligible effects on these measurements.

### 3.3.2 EMCAL Energy Calibration

The EMCAL absolute energy scale is calibrated using an  $\eta$ -dependent calibration to the  $\pi^0 \rightarrow \gamma\gamma$  mass peak. This calibration is performed in-situ using the same beam data as is used for the physics analyses and is calibrated to a mass target value determined from simulation. This simulation-based target mass is determined from a full detector simulation of Au+Au collisions generated with HIJING [15] and  $p+p$  collisions generated with PYTHIA8 [16, 17] passed through a GEANT-4 [18] simulation of the sPHENIX detector and digitized using the sPHENIX digitization chain. The calibration procedure contains two steps: first a relative calibration based on the tower slope method is applied to the EMCAL towers to enforce  $\phi$  symmetry and eliminate tower-by-tower gain differences. In the tower slope method, each tower spectra is fit to the reference spectra using the fit function  $A \times f(gE)$ , where  $A$  is a scale factor and  $g$  is the gain parameter, in the tower energy

region between 0.2 and 0.8 GeV. This procedure is performed twice with a QA procedure between iterations to remove outlier towers with gain values outside 5 standard deviations of the mean. The tower slope mean and standard deviation values are then recalculated after removing outliers and tower by tower gain values are extracted again from the fit to the reference spectra.

Second, the absolute calibration to the  $\pi^0 \rightarrow \gamma\gamma$  mass peak is performed using EMCAL clusters composed of continuous towers with energies exceeding 70 MeV and results are combined for EMCAL towers in each  $\eta$  slice. Performing this  $\phi$  based relative calibration and then  $\eta$  based absolute calibration allows for high statistics in performing the absolute calibration while still accurately calibrating each tower in both  $\phi$  and  $\eta$ . The  $\pi^0$  mass peak formed from the EMCAL di-cluster invariant mass distribution is fit with a Gaussian plus third order polynomial background function to extract the mass peak position and width for each  $\eta$  slice. The extracted  $\pi^0$  mass peak position for each  $\eta$  slice is compared to the simulation-based target mass value for that  $\eta$  slice and the absolute calibration is updated according to the ratio of the target mass over the observed mass. This procedure is iterated through many times (20-30) until sub-statistical fluctuations in the observed  $\pi^0$  mass peak position are achieved.

For the EMCAL absolute energy scale calibration for the Run 2024 Au+Au dataset, data to simulation comparisons of the  $\pi^0$  distribution showed that the  $\pi^0$  mass width was larger in data than simulation when using nominal HIJING events and the default sPHENIX GEANT-4 simulation and digitization. The data to simulation disagreement in the  $\pi^0$  mass width can be seen in Figure 3.9. Additionally,  $\pi^0$  mass peak position used for the EMCAL calibration is shifted in both data and simulation from the Particle Data Group value [19] because of effects from the convolution of the falling energy spectrum and the resolution in the energy response of the EMCAL clusters used for the calibration.

To understand effects on the calibration from the data's wider EMCAL energy resolution and improve the data to simulation agreement in the  $\pi^0$  mass width, a EMCAL cluster energy smearing procedure was implemented in simulation. This smearing procedure applied an additional energy independent gaussian smearing term to the EMCAL cluster energies in simulation. To find the cor-

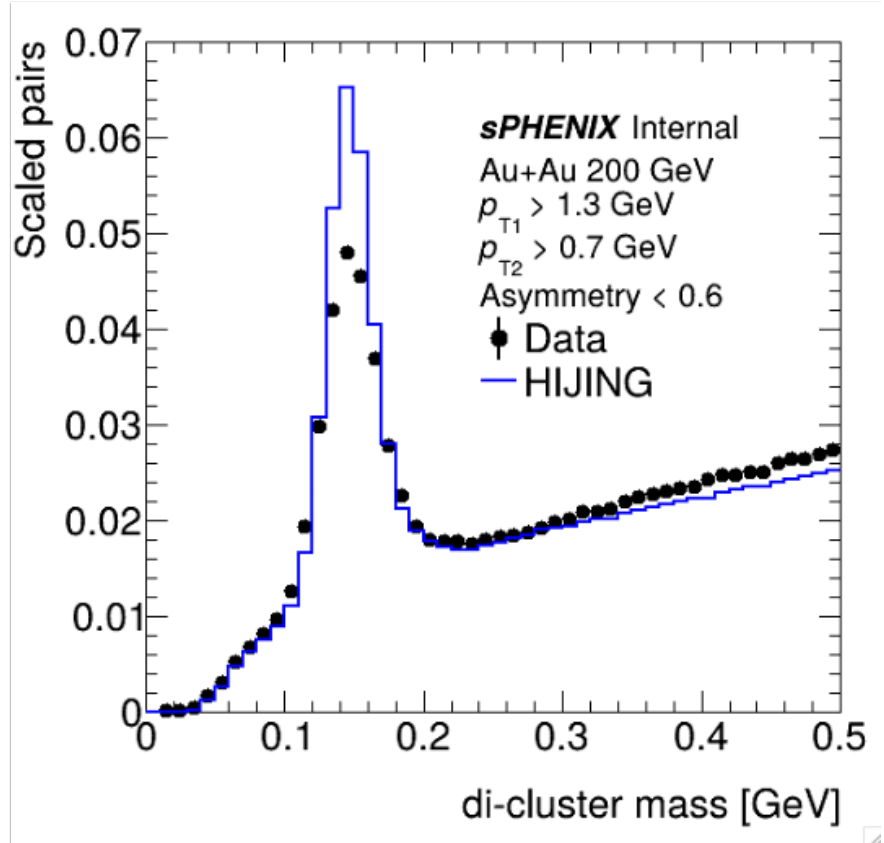


Figure 3.9: EMCAL di-cluster invariant mass distribution from Run 2024 Au+Au data (black points) and geant-4 simulation of **HIJING** events (blue histogram) before cluster energy smearing.

rect width for the smearing term, an iterative procedure was performed starting from the quadrature difference of the  $\pi^0$  mass width in data and simulation. The smearing width was adjusted until convergence of the  $\pi^0$  mass width in simulation to that in data was reached. After two iterations of this procedure, a smearing width of 8.4% on the  $\pi^0$  mass peak corresponding to a smearing width of 11.9% ( $\sqrt{2} * 8.4\%$ ) on the EMCal cluster energies was found to give good agreement with the  $\pi^0$  mass width in data. Figures 3.10 show the  $\pi^0$  mass peak position and width as a function of cluster  $\eta$  slice with and without the simulation EMCal cluster energy smearing and Figure 3.11 shows the good agreement in the EMCal di-cluster distribution between data and simulation with the EMCal cluster energy smearing.

Additional studies in both data and simulation were performed to better understand the source of the wider  $\pi^0$  mass peak width in data. These studies included studying the extracted  $\pi^0$  mass peak value and width from the calibration procedure as a function of  $\pi^0 p_T$ , studying the effects of the EMCal tower noise on the tower energy resolution, and studying variations in the calibration parameters including the cluster tower energy threshold and centrality selection.

The  $\pi^0$  mass peak value and width as a function of  $\pi^0 p_T$  before and after the EMCal cluster energy smearing is shown in Figure 3.12. While there is some small  $p_T$  dependence in the  $\pi^0$  mass peak and width, this residual dependence is seen in all data and simulation samples and should be due to the fitting procedure which is optimized for low  $p_T \pi^0$ 's which dominate the calibration process rather than an inherent  $p_T$  dependence. The di-cluster invariant mass distributions for different  $\pi^0 p_T$  bins are shown with the gaussian plus polynomial background fit in Figure 3.13.

Energy resolution effects from the EMCal tower noise were studied in simulation by turning off and on the realistic EMCal tower noise in the digitization step of the simulation. Figure 3.14 shows a 3.5% effect on the EMCal tower energy resolution from the inclusion of realistic EMCal tower noise for towers  $\sim 1GeV$  which dominate the calibration cluster candidates. This effect is small in comparison to the 11.9% EMCal cluster energy smearing needed to achieve good agreement between data and simulation in the  $\pi^0$  mass peak width.

Finally studies of variations in the calibration parameters including the cluster tower energy

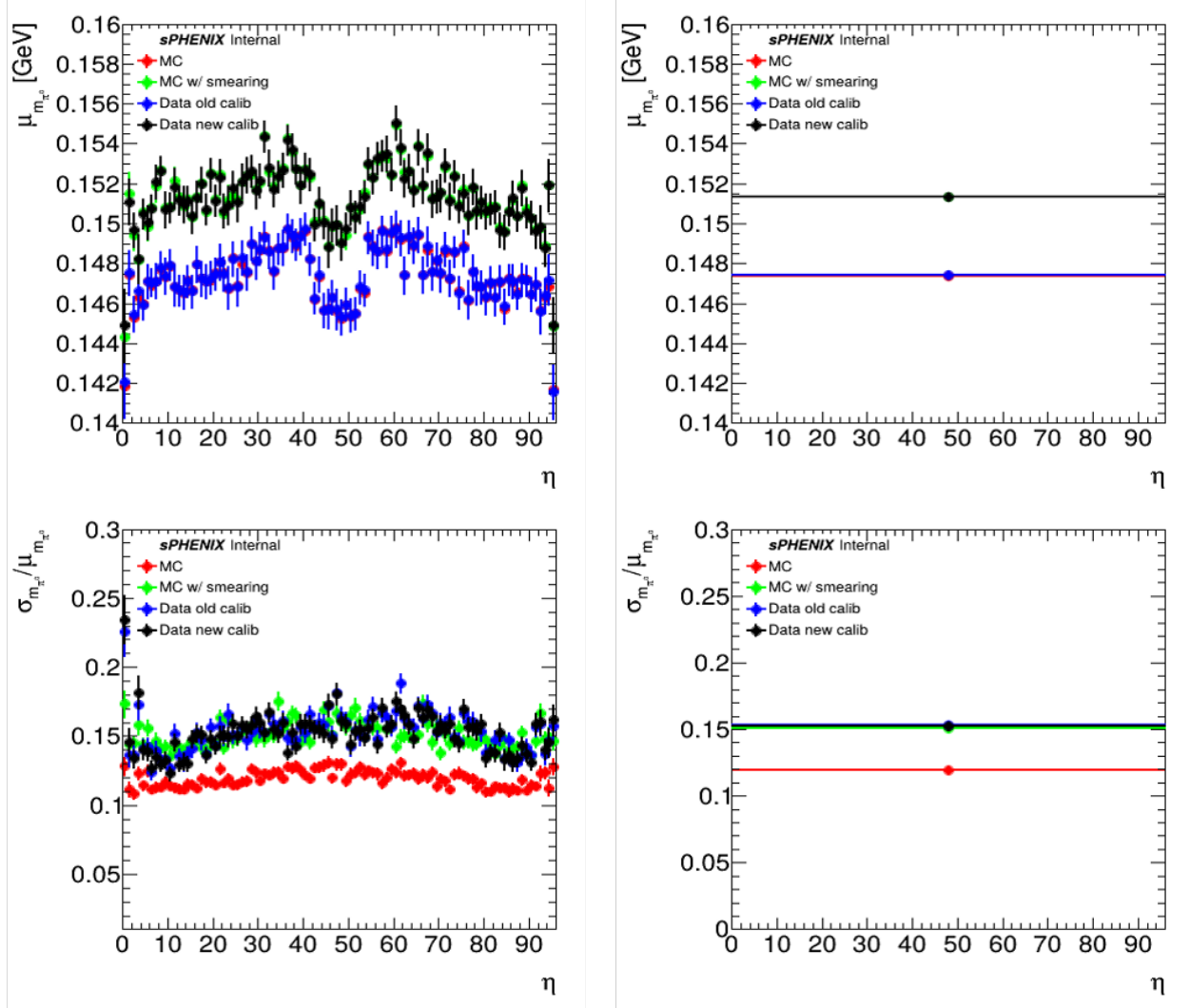


Figure 3.10: EMCAL  $\pi^0$  mass peak position (top) and relative width (bottom) for simulation (red), simulation with cluster energy smearing (green), data calibrated to the un-smeared simulation (blue) and data calibrated to the smeared simulation (black). Left plots show quantities as a function of cluster  $\eta$  slice and right plots show the  $\eta$  averaged quantities for easy comparison.

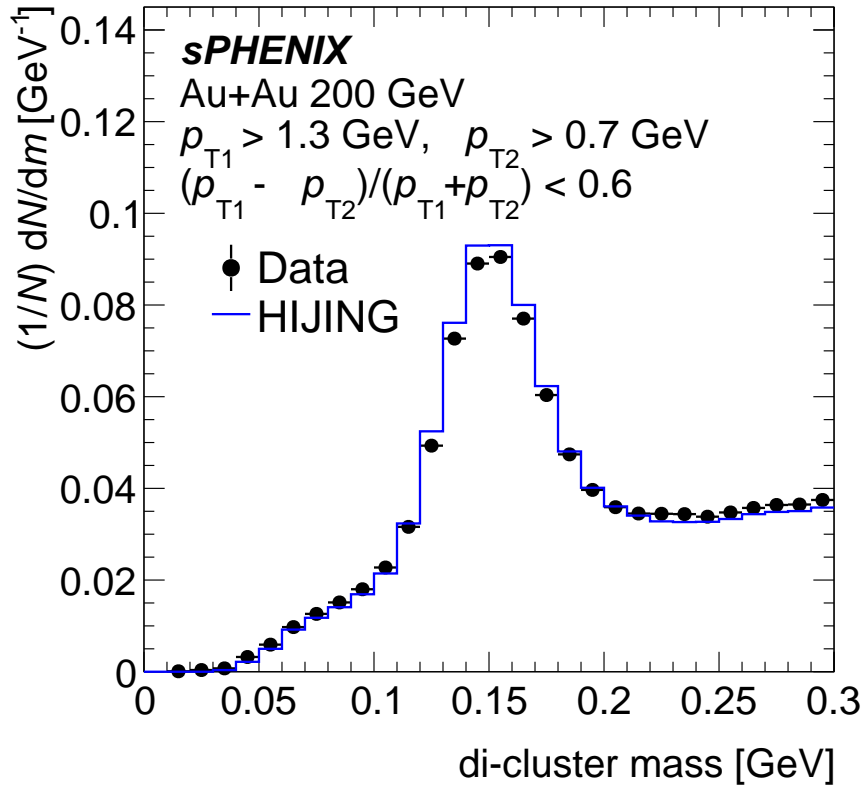


Figure 3.11: Final EMCAL di-cluster invariant mass distribution from Run 2024 Au+Au data (black points) and geant-4 simulation of HIJING events (blue histogram).

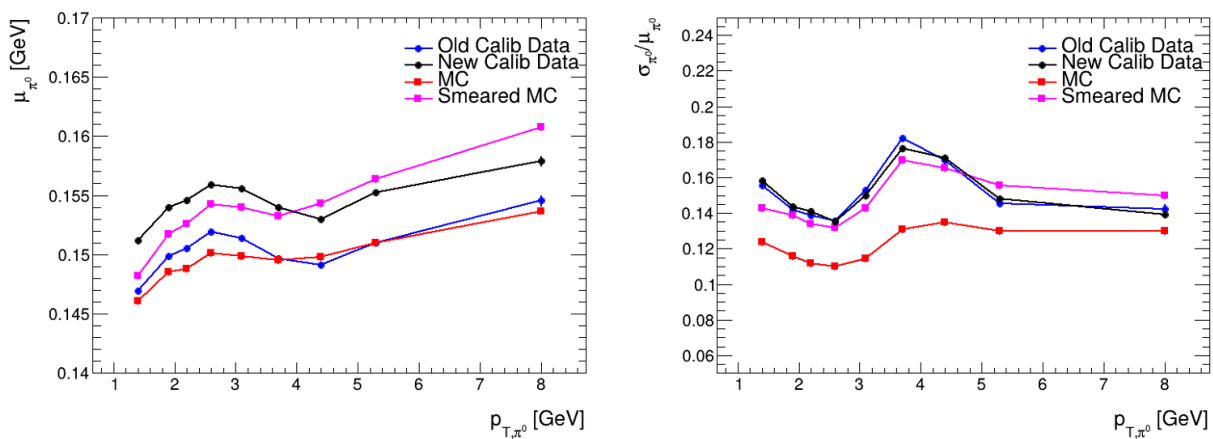


Figure 3.12: EMCAL  $\pi^0$  mass peak position (left) and relative width (right) as a function of  $\pi^0 p_T$  for simulation (red), simulation with cluster energy smearing (pink), data calibrated to the un-smeared simulation (blue) and data calibrated to the smeared simulation (black).

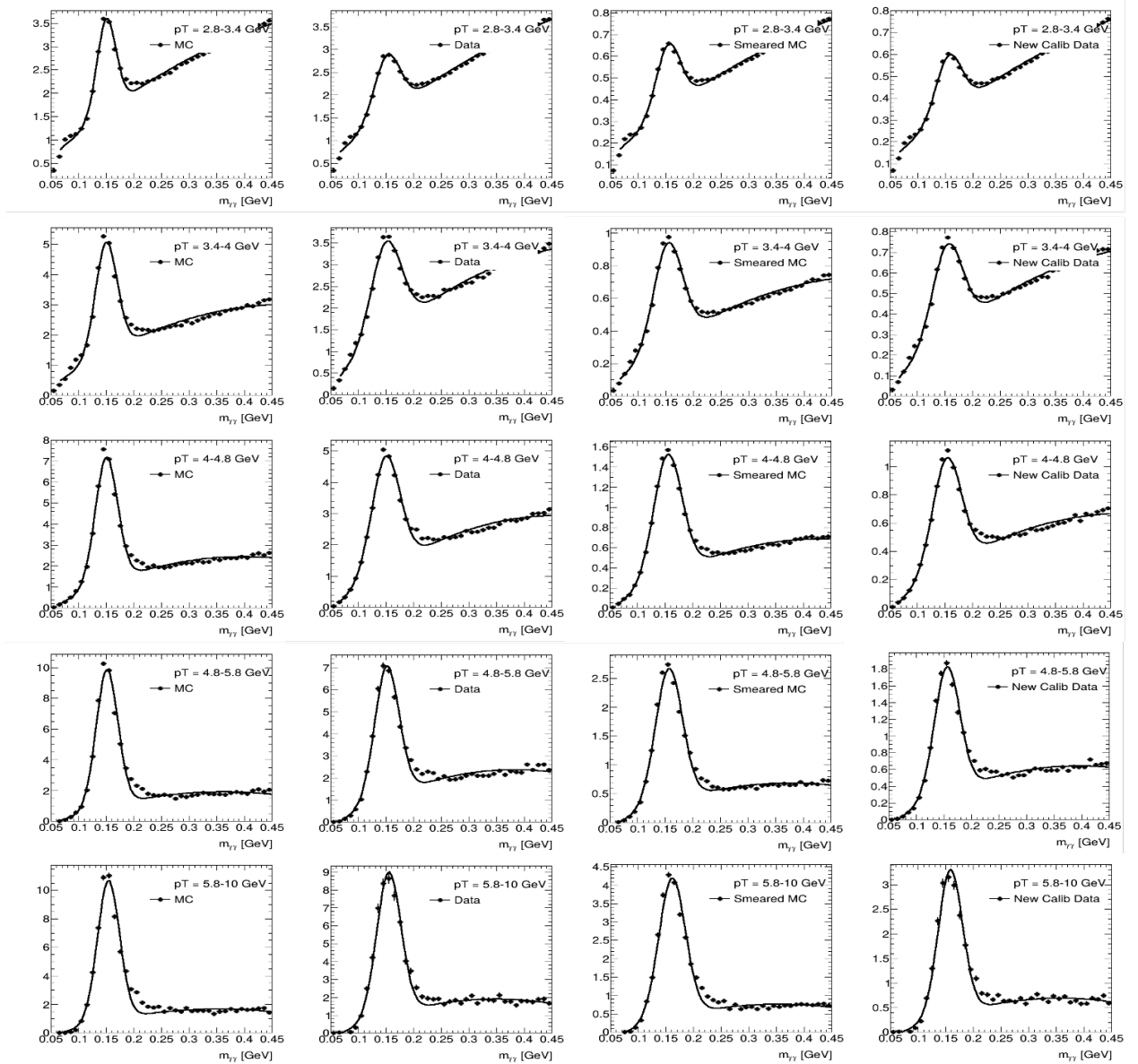


Figure 3.13: EMCAL di-cluster invariant mass distributions for bins of  $\pi^0$   $p_T$  for simulation (left), simulation with cluster energy smearing (left middle), data calibrated to the un-smeared simulation (right middle) and data calibrated to the smeared simulation (right). Fits to the  $\pi^0$  mass peak using Gaussian plus polynomial background are included.

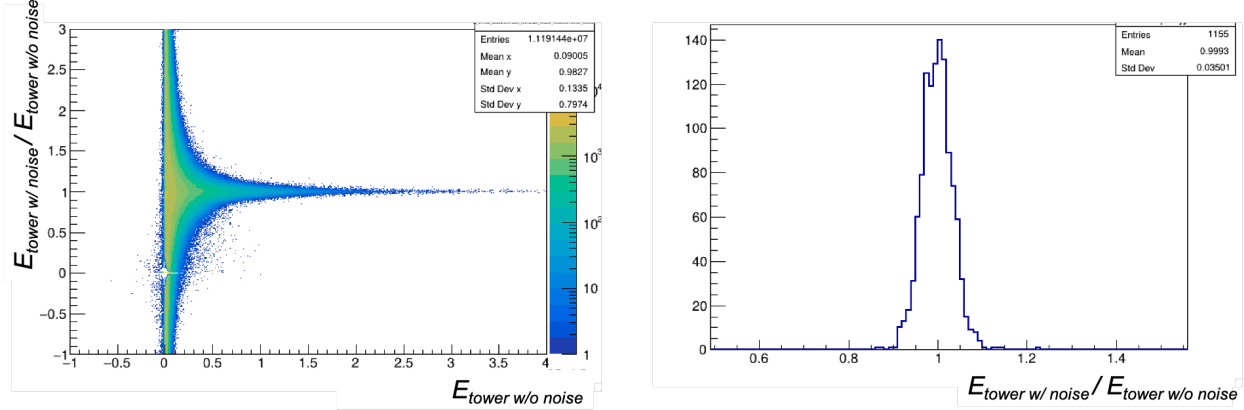


Figure 3.14: Left: Ratio of EMCal tower energies with and without inclusion of realistic EMCal tower noise as a function of EMCal tower energies without inclusion of realistic EMCal tower noise. Right: Profile of ratio of EMCal tower energies with and without inclusion of realistic EMCal tower noise for EMCal tower energies around 1 GeV.

threshold and centrality selection were performed. Figures 3.15 and 3.16 show the effects of varying the cluster tower energy threshold and centrality selection on the extracted  $\pi^0$  mass peak value and width in both data and simulation. When varying the cluster tower energy thresholds, small deviations (< 2%) on the extracted  $\pi^0$  mass peak value and width are seen from these variations and the scale and trend of these variations are well matched between data and simulation. The centrality selection in simulation and data is set as a percentile cut on the total event EMCal cluster multiplicity. The centrality selection in simulation was varied to match the data absolute-scale total event EMCal cluster multiplicity cut and was found to have negligible effects on the  $\pi^0$  mass peak position and width.

All variations in cluster reconstruction parameters, centrality selection and tower noise simulation were not able to explain the simulation to data disagreement in the  $\pi^0$  mass width without the inclusion of the EMCal cluster energy smearing procedure in simulation. Therefore, a conservative systematic uncertainty of 2.6% derived from the variation between the  $\pi^0$  mass peak position with and without the EMCal cluster energy smearing procedure is included in the uncertainties on the EMCal absolute energy scale calibration.

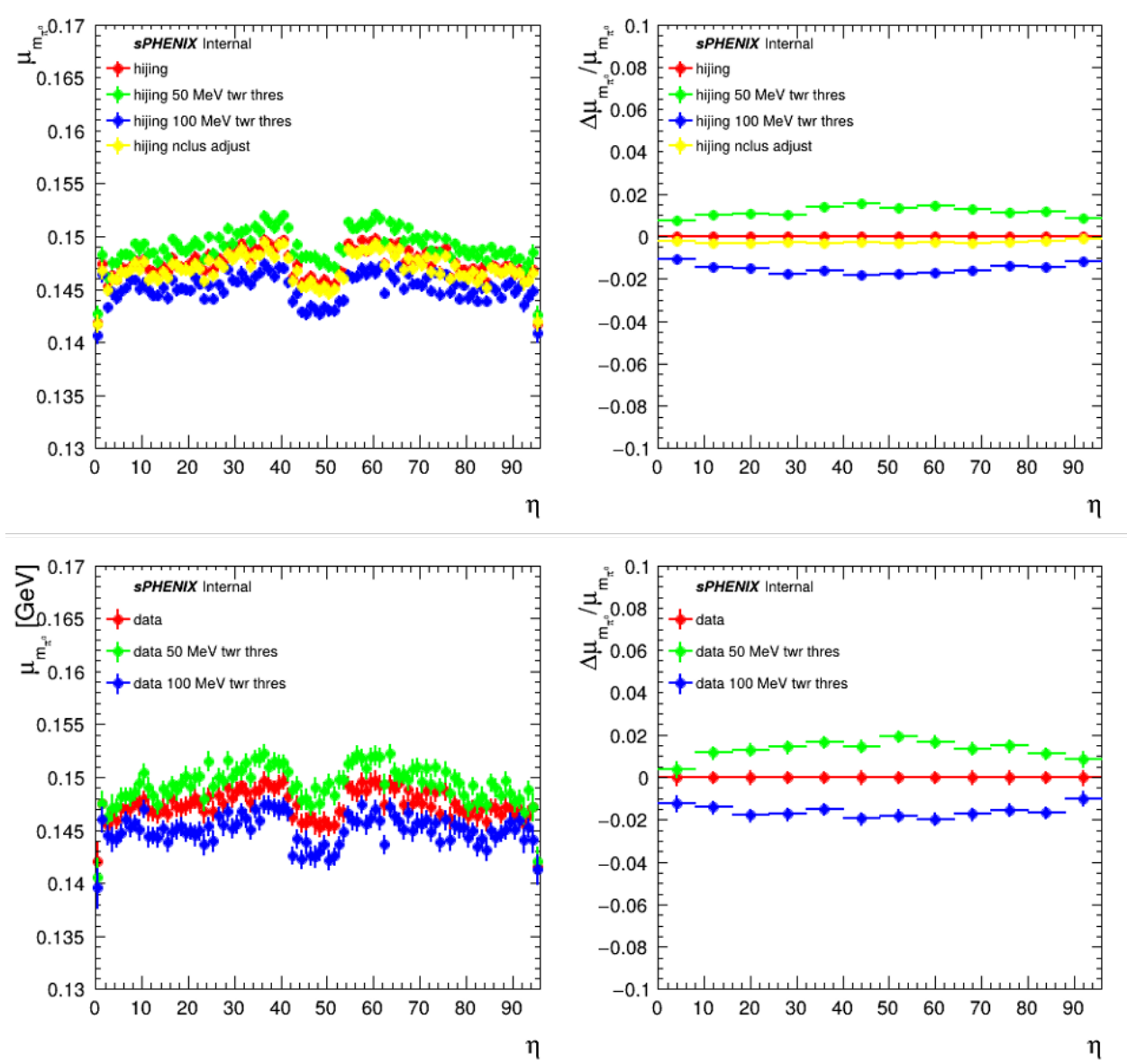


Figure 3.15: EMCAL  $\pi^0$  mass peak position value (left) and variation from nominal (right) as a function of  $\eta$  for nominal result (red), variations in cluster tower energy thresholds (green, blue), and variation in simulation centrality selection (yellow). Variation results for simulation are shown in top plots and for data are shown in bottom plots.

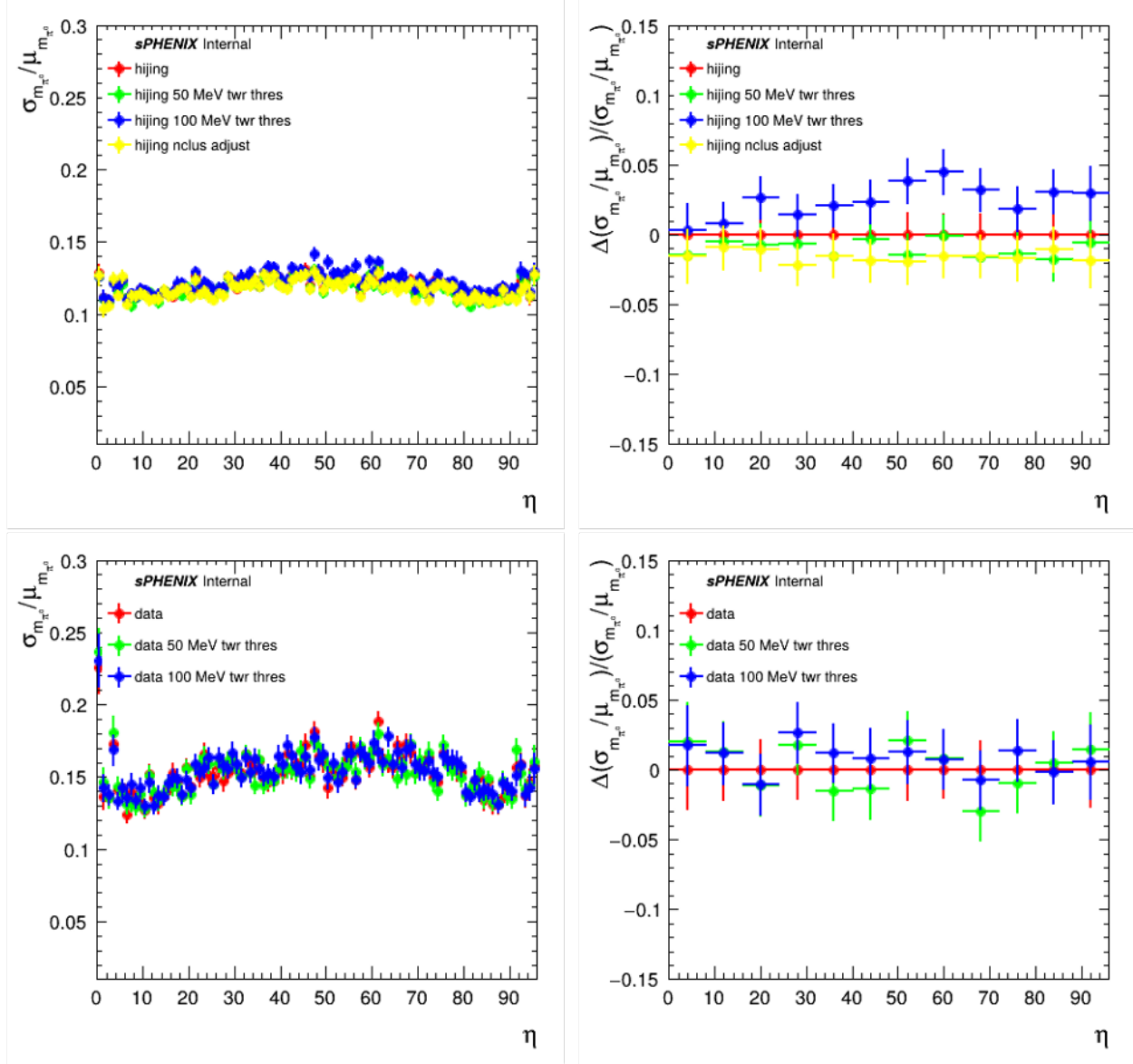


Figure 3.16: EMCal  $\pi^0$  mass peak relative width value (left) and variation from nominal (right) as a function of  $\eta$  for nominal result (red), variations in cluster tower energy thresholds (green, blue), and variation in simulation centrality selection (yellow). Variation results for simulation are shown in top plots and for data are shown in bottom plots.

### 3.3.3 HCal Energy Calibration

The IHCal and OHCal are both calibrated to the electromagnetic energy scale using the minimum ionizing particle (MIP) energy depositions from cosmic ray muons from data taken during no-beam period. These cosmics runs are taken throughout the year-long data-taking period. Therefore, it is expected that the detector conditions are fairly consistent between cosmics and beam running and any small time-dependent detector condition effects on gain variations should be accounted for in the calibration from cosmics data. To collect an unbiased sample of cosmic ray muon events, a single OHCal tower trigger with a threshold well below the MIP peak is used. A simulation dataset using cosmic ray muons generated with EcoMug [20] and propagated through a GEANT-4 [18] simulation of the sPHENIX detector is used to model in simulation the angular distribution of cosmic rays seen by the sPHENIX HCals. In both data and simulation, a set of offline cuts are applied to select muon events that propagate through a single HCal tower in the azimuthal direction depositing energy in a majority of the tower's scintillating tiles. These offline cuts include an isolation cut on the energy surrounding the tower in  $\eta$  and a requirement of energy deposited in the neighboring towers in  $\phi$ . A comparison between data and simulation after these offline cuts of the MIP energy distribution for an OHCal tower can be found in Figure 3.17. Since this selection requires events where the muon traverses a majority of the tower's scintillating tiles, it results in a narrow, characteristic MIP energy peak needed for a precise calibration.

An additional HCal calibration step of a tower-slope correction is applied to account for inconsistencies in the angular distribution of cosmic rays in the cosmic data simulation; here a relative calibration is applied to HCal towers using the assumptions of  $\phi$  symmetry and that the absolute cosmics-based calibrations of the HCal towers on the sides of the detectors with very high statistics are accurate. Finally, an additional sampling fraction factor is applied to calibrate the measured scintillator MIP energy distribution to an estimate of the energy in the full HCal tower (scintillator and absorber material). This sample fraction value was determined in the sPHENIX GEANT-4 simulation using high- $E_T$  single hadrons and validated by test beam studies [11].

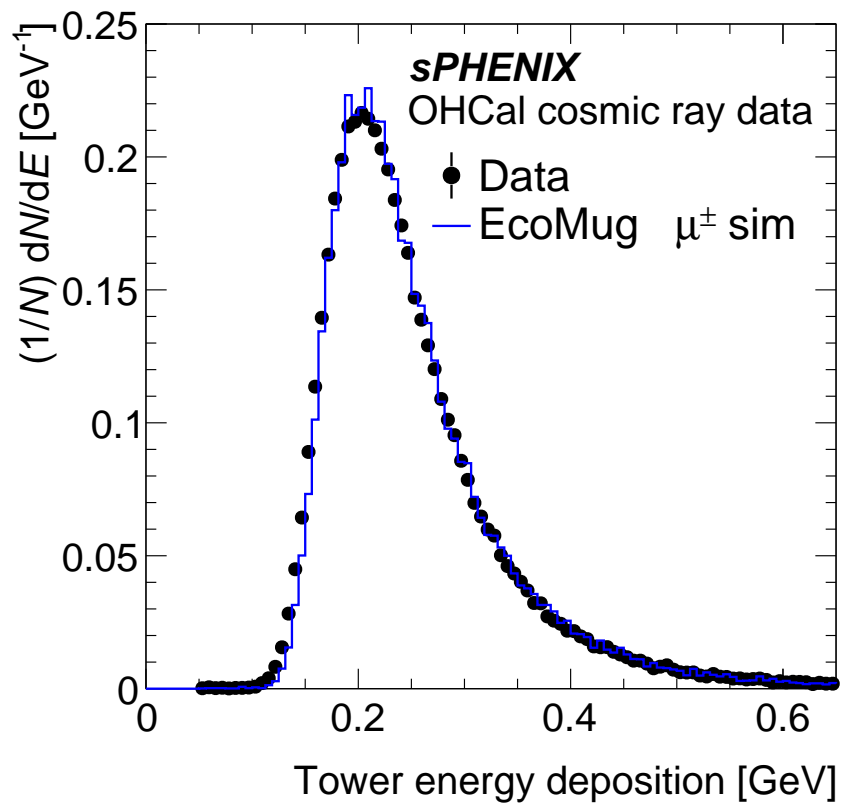


Figure 3.17: Comparison of OHCal tower MIP energy distribution from cosmic ray data (black) and GEANT-4 simulation of EcoMug generated cosmic ray muons (blue histogram) for an example tower used in the absolute energy scale calibration. The characteristic MIP peak is clearly visible around 250 MeV.

### 3.3.4 Calorimeter Zero Suppression and Cross Calibration

The effect of tower reconstruction via fitting to the calorimeter waveform template versus zero suppression algorithm as well as the application of an additional cross calibration factors for zero suppressed towers was extensively studied since the low energy towers are a significant contributor to soft physics analyses like the  $dE_T/d\eta$  and underlying event measurements. An additional calibration was applied to the ZS tower energies to account for the ZS algorithm, waveform sample 6 - sample 0, underestimating the tower energy. The calorimeters on the whole are timed in at sample 6, however for multiple reasons including differences in trigger latching time samples, intra-sector cable lengths and tower distances to the collision points, on the tower by tower level, a tower may not be timed in exactly at sample 6. While the template fit has little to no constraints within the waveform length on the signal timing when looking for the signal peak, the ZS algorithm expects the signal peak to be timed in exactly at sample 6. Therefore, a cross calibration is applied to the zero suppressed waveforms to account for shifts in the tower-by-tower mean time of signal peaks. This ZS cross calibration is determined using the ratio of  $\frac{\overline{ADC}_{Template\ fit}}{ADC_{ZS}}$  for well defined signals, signals with  $ADC_{Template\ fit} = [200,2000]$  ADC for EMCal and  $ADC_{Template\ fit} = [100,2000]$  ADC for HCals. These cross calibration factors are determined on a tower-by-tower and run-by-run basis to account for tower-by-tower timing differences.

#### $ADC_{Template\ Fit}$ versus $ADC_{Sample\ 6 - sample\ 0}$

Two methods are used to study effect of applying ZS by comparing the energy value of a tower from the template fit versus the energy value of the tower from sample 6 – sample 0. First by looking at the correlation of  $ADC_{Template\ fit}$  to  $ADC_{Sample\ 6 - sample\ 0}$  to look at the energy dependence on the relationship between the template fit and ZS energy values. Second by looking at the mean ratio of  $ADC_{Template\ fit}/ADC_{Sample\ 6 - sample\ 0}$  for each tower entry in a set energy range to look for tower by tower effects on the relationship between the template fit and ZS energy values.

For EMCal  $ADC_{Template\ fit}$  to  $ADC_{Sample\ 6 - sample\ 0}$  correlation plot in Figure 3.18 (upper left), there is a main trendline at 1, a broader trendline below 1, and additional structure in region

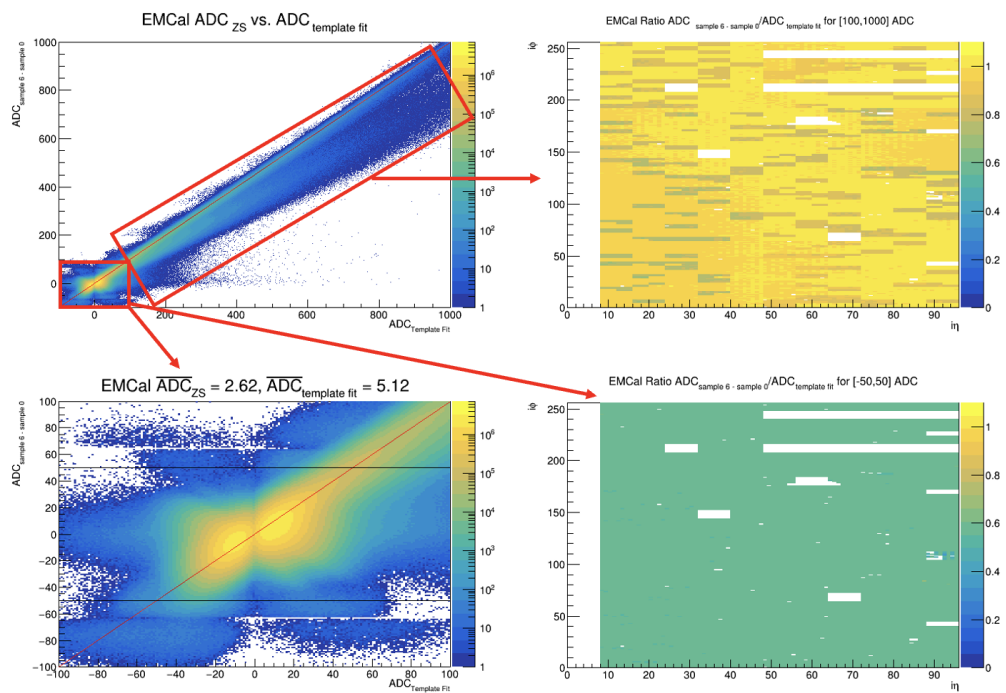


Figure 3.18: Comparison of EMCal waveform processing with zero suppression versus template fit. Correlation between tower's ADC value from ZS versus from template fit shown in left plots for two different ADC ranges  $[-100, 1000]$  ADC (top left) and  $[-100, 100]$  ADC (bottom left). Ratio of ADC value from ZS versus ADC value from template fit on a tower by tower basis shown in right plots for two different ranges  $[100, 1000]$  ADC (top right) and  $[-100, 100]$  ADC (bottom right).

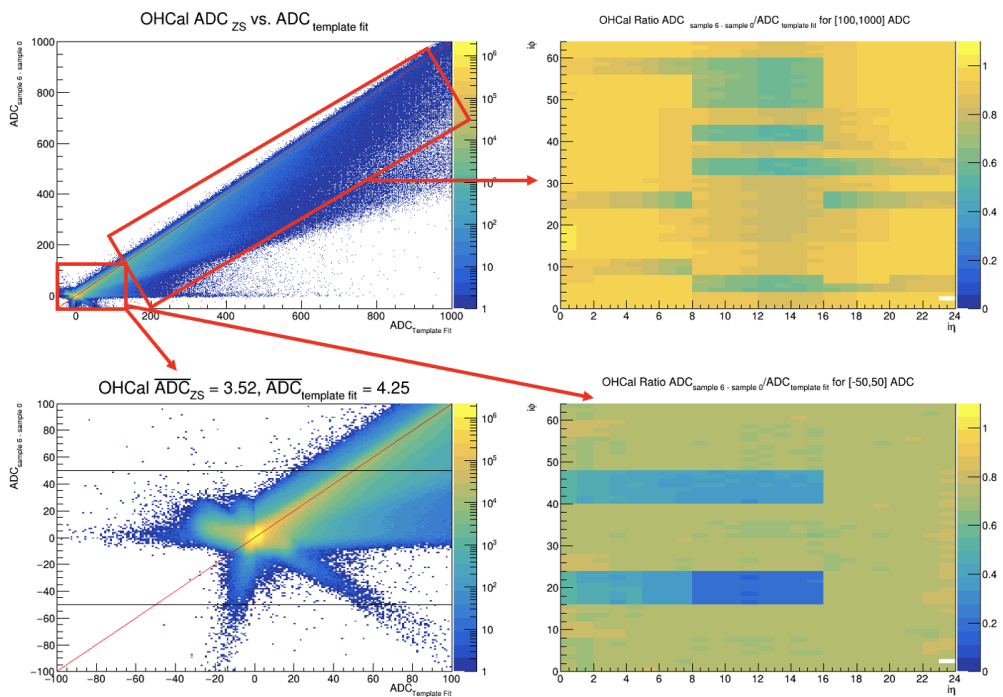


Figure 3.19: Comparison of OHCal waveform processing with zero suppression versus template fit. Correlation between tower's ADC value from ZS versus from template fit shown in left plots for two different ADC ranges  $[-100, 1000]$  ADC (top left) and  $[-100, 100]$  ADC (bottom left). Ratio of ADC value from ZS versus ADC value from template fit on a tower by tower basis shown in right plots for two different ranges  $[100, 1000]$  ADC (top right) and  $[-100, 100]$  ADC (bottom right).

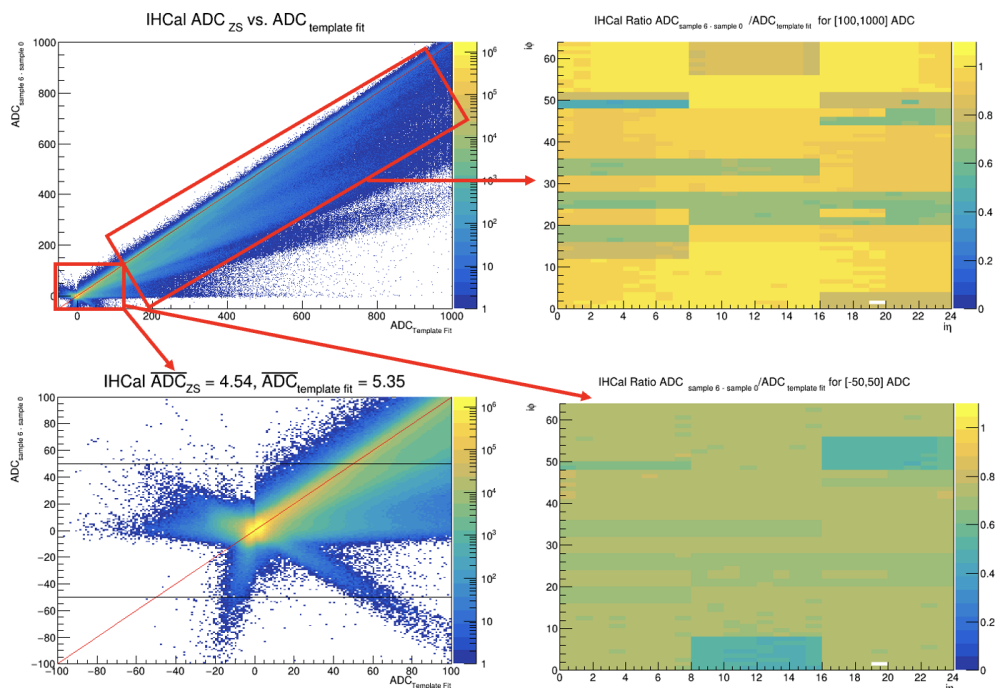


Figure 3.20: Comparison of IHCAL waveform processing with zero suppression versus template fit. Correlation between tower's ADC value from ZS versus from template fit shown in left plots for two different ADC ranges  $[-100, 1000]$  ADC (top left) and  $[-100, 100]$  ADC (bottom left). Ratio of ADC value from ZS versus ADC value from template fit on a tower by tower basis shown in right plots for two different ranges  $[100, 1000]$  ADC (top right) and  $[-100, 100]$  ADC (bottom right).

below 100 ADC. Additionally, in the region below 100 ADC in the EMCal  $ADC_{\text{template fit}}$  to  $ADC_{\text{sample 6 - sample 0}}$  correlation plot, there are both correlated and anti-correlated trends of the template fitting versus zero suppression algorithm. For OHCal  $ADC_{\text{template fit}}$  to  $ADC_{\text{sample 6 - sample 0}}$  correlation plot in Figure 3.19 (upper left) there are the same trends as EMCal correlation plot, namely a band at 1, a broader band below 1 and structure at low energy. However, the band below 1 for the OHCal is broader than in the EMCal case. Additionally, in the OHCal case, there are still the correlated and anti-correlated trendlines for the processing of low energy waveforms using the template fit versus the ZS method. Finally, the IHCal  $ADC_{\text{template fit}}$  to  $ADC_{\text{sample 6 - sample 0}}$  correlation plot has the same trends as EMCal/OHCal correlation plot (band at 1, broader band below 1, structure at low energy).

Further investigation into the correlated and anti-correlated trendlines seen in the low ADC region was conducted using the OHCal and EMCal waveforms. When selecting for waveforms which fit into the anti-correlated band, namely with a positive ADC value from processing with the template fit and a negative ADC value from processing with the ZS method and vice versa, the majority of the events in this anti-correlated band were abnormal waveforms like the ones shown in Figure 3.21. Figure 3.21 shows a waveform decreasing (left)/increasing (right) across the full timing window of the waveform and exhibiting some kind of long range or multi time sample noise in addition to single sample noise. This fully increasing/decreasing noise behavior is fit by the template fit to be the tail of a waveform peak, therefore in the increasing case, the template fit returns a positive ADC value and a peak timing between the 0-4th time sample, and in the decreasing case, the template fit returns a negative ADC value expecting that this is the tail of an inverted peak also with a peak timing between the 0-4th time sample. The fully decreasing waveform processed by template fit with value of 18.9 ADC and processed with ZS algorithm with value of -10 ADC, while the fully increasing waveform processed by template fit with value of -20.5 ADC and processed with ZS algorithm with value of 11 ADC.

Understanding how the template fit processes these waveforms with long range noise helps to understand the structure and scale of Figures 3.18 (bottom right) and 3.19 (bottom right). These

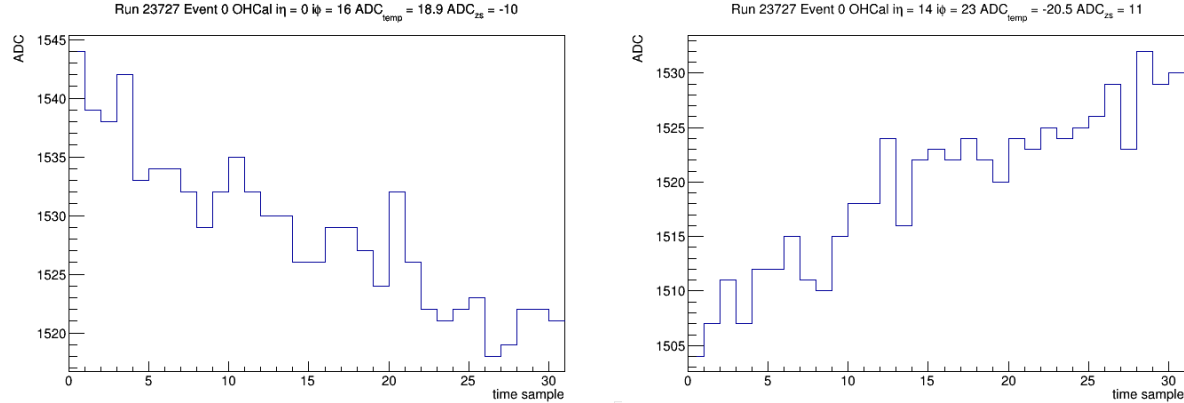


Figure 3.21: Examples of noisy waveforms from beam data.

plots show the mean ratio of ADC distribution in region [-50,50] is lower for ZS distribution than template fit distribution. For the EMCAL, this mean ratio of  $ADC_{\text{template fit}}/ADC_{\text{sample 6 - sample 0}}$  in low energy range (+/-75 MeV) show a consistent ratio of 0.57. This ratio should be related to the competing effects at low energy of correlated energy values found from processing with the template fit and ZS on waveforms with low energy signals and anti-correlated energy values found from processing waveforms with long range noise using the template fit and ZS. The OHCAL mean ratio of  $ADC_{\text{template fit}}/ADC_{\text{sample 6 - sample 0}}$  in low energy range (+/-150 MeV) is around 0.74 but has two blue areas that correspond to 4 ADC boards with high pedestal RMS (around 10 ADC), that seem to be main contributors to the anti-correlation band seen in the full detector correlation plot. Once again the two trends compete with one another at low energy with more noisy boards having a lower mean ratio due to the larger contribution of anti-correlated noise and less noisy boards having a higher mean ratio due to the smaller contribution of anti-correlated waveforms. The IHCAL mean ratio of  $ADC_{\text{template fit}}/ADC_{\text{sample 6 - sample 0}}$  in low energy range (+/-25 MeV) has 2 blue shaded areas correspond to 2 ADC boards with high pedestal RMS (around 6 ADC) which exhibit the same behavior as the OHCAL noisy boards.

The absolute calibration established for all three calorimeters is using the template fit where the peak time is a free parameter. Since the ZS method does not take the timing as a free parameter, a cross calibration is necessary to account for tower by tower timing differences which are easily handled by the template fit but are not handled by the ZS method. Specifically the ratio of ADC

values found using the ZS method and the ADC values found using the template fit are used to determine the energy values in GeV that correspond to the ADC values extracted from the ZS algorithm.

To find this cross calibration, the  $ADC_{\text{template fit}}/ADC_{\text{sample 6 - sample 0}}$  ratio for well defined waveforms above the noise contributions is used. This corresponds to the band structure at 1 and lower band structure below 1 seen in the  $ADC_{\text{template fit}}$  to  $ADC_{\text{sample 6 - sample 0}}$  correlation plots (Figs. 3.18, 3.19, 3.20 (top left)). By mapping these trends on to the tower by tower mean ratio of  $ADC_{\text{template fit}}/ADC_{\text{sample 6 - sample 0}}$  in higher energy range [100,1000] ADC (Figs. 3.18, 3.19, 3.20 (top right)), for the EMCal, most towers have a ratio value of nearly 1 with some parts of the detector having a value around 0.8, likely from these parts of the detector not being timed in exactly at time sample 6. These towers contribute to the band below 1 in the correlation plot. There are similar results in the OHCal and IHCal, with parts of the detector having a ratio of 1 and towers timed in at time sample 6, and other parts of the detector being slightly out of time, lowering the ratio and contributing to the large band below 1 seen in the OHCal and IHCal  $ADC_{\text{template fit}}$  to  $ADC_{\text{sample 6 - sample 0}}$  correlation plots. Additionally, the structure in mean ratio of  $ADC_{\text{template fit}}/ADC_{\text{sample 6 - sample 0}}$  which somewhat corresponds to different cable lengths of OHCal, once again pointing towards this ratio be influenced by timing differences between different parts of the detector.

These tower by tower ratios are used as a cross calibration for the energy in GeV from the ZS waveform processing method. To find the energy of a waveform processed with the ZS method, we use the following equation:

$$E_{\text{ZS}} = ADC_{\text{ZS}} * C_{\text{Template fit}} * \frac{\overline{ADC}_{\text{Template fit}}}{\overline{ADC}_{\text{ZS}}} \quad (3.1)$$

where  $C_{\text{Template fit}}$  is the tower by tower absolute energy calibration factor from either the HCal cosmics calibration or EMCal calibration from the  $\pi^0$  mass peak and  $\frac{\overline{ADC}_{\text{Template fit}}}{\overline{ADC}_{\text{ZS}}}$  is the tower by tower ZS cross calibration factor previously described and shown in Figs. 3.18, 3.19, 3.20 (top

right).

### ZS + template fit method for calorimeter tower reconstruction

Through in-depth studies of the ZS and template fit waveform processing methods, it is now understood that the low energy region of our tower energy spectra is quite noisy and this noise is processed differently using the template fit versus ZS method. To eliminate the positive bias derived from the template fit processing of noisy waveforms, a ZS + template fit method is implemented for processing calorimeter towers. In this ZS + template fit processing method, a threshold ADC value is established which is checked against a waveform's sample 6 - sample 0 ADC value. If the waveform's ZS value falls below the threshold ADC value, the waveform is processed using the value from sample 6 - sample 0 and if the waveform's ZS value is above the threshold ADC value, the waveform is processed using the template fit method.

The goal of using the ZS + template fit method is to fully process the calorimeter *noise* waveforms with the ZS method so that they do not incur a positive bias from the template fitting. This method was commissioned using beam data from Run 2023. A range of thresholds from 10 to 50 ADC is tested to find at what point the minimum bias distribution of calorimeter total  $E_T$  value, for example, becomes robust to the ZS + template fit processing method, indicating that there are no longer noise contributions included in the offset or pedestal of the total calorimeter energy. Figure 3.22 shows the effect of applying various ZS thresholds on the minimum bias distribution of the total  $E_T$  of each calorimeter.

Applying any ZS threshold has the largest effect on the EMCAL total  $E_T$  distribution; there is a large decrease in the offset of the total  $E_T$  distribution once any low energy waveforms are processed with the ZS method instead of the template fit. Interestingly, for low ZS thresholds, like 10 ADC, the EMCAL total  $E_T$  distribution peaks at below 0 GeV and then for increasing thresholds, the total  $E_T$  distribution increases and finally stabilizes at 5 GeV for ZS thresholds of 30 ADC and above. For the ZS thresholds of 10 and 20 ADC, some of the noise is still being processed using the template fit. However, recalling the waveforms in Figure 3.21, the waveform that is uniformly

decreasing will be always be fit with the ZS method, resulting in a negative energy contribution to the calorimeter total  $E_T$  while the waveform that is uniformly increasing when fit with the template fit method because its ZS value is above the threshold will also result in a negative energy contribution to the total  $E_T$  as this waveform processed with the template fit is seen as the tail of an inverted peak. Therefore, when processing all of the waveforms with decreasing long range noise with the ZS method and some of the waveforms with increasing long range noise with the template fit method, there is an overall shift of the total  $E_T$  distribution in the negative energy direction. In raising the ZS threshold, more of these increasing noise waveforms are then processed with the ZS method, and the total  $E_T$  rises and finally stabilizes around a threshold of 30 ADC.

There is very little impact on the IHCAL total  $E_T$  distribution and a modest decrease of the offset of the OHCal total  $E_T$  distribution of about 2 GeV leaving the offset of the OHCal total  $E_T$  distribution processed with the ZS + template fit method between 0 and 1 GeV. Additionally, for the OHCal total  $E_T$  distribution, there is very little change in the distribution for ZS thresholds of 20 ADC and higher.

The reconstructed  $dE_T/d\eta$  measurement from each calorimeter subsystem is also an excellent tool for investigating calorimeter calibration and reconstruction effects. This measurement will be outlined in detail in Chapter 4, but for the purposes of interpreting the template fit + ZS method for calorimeter waveform reconstruction, the reconstructed-level  $dE_T/d\eta$  is the sum of transverse energy from all towers in an  $\eta$  slice of the calorimeter, ( $\Sigma E_{T,tower}(\eta)$ ). The effect of applying ZS and the ZS cross calibration factors on the reconstructed-level calorimeter  $dE_T/d\eta$  is shown in Figures 3.23, 3.24 and 3.25. There is large effect on the reconstructed-level EMCAL  $dE_T/d\eta$  value when applying any threshold of zero suppression. However, there is little effect on the reconstructed-level EMCAL  $dE_T/d\eta$  measurement from applying the ZS cross calibration factors since the majority of the EMCAL is timed in uniformly and most EMCAL towers have cross calibration factors very close to 1.

In Figure 3.24, there is a small effect on the reconstructed-level IHCAL  $dE_T/d\eta$  from applying any ZS threshold. Additionally, when a ZS cross calibration factor is not applied, the reconstructed-

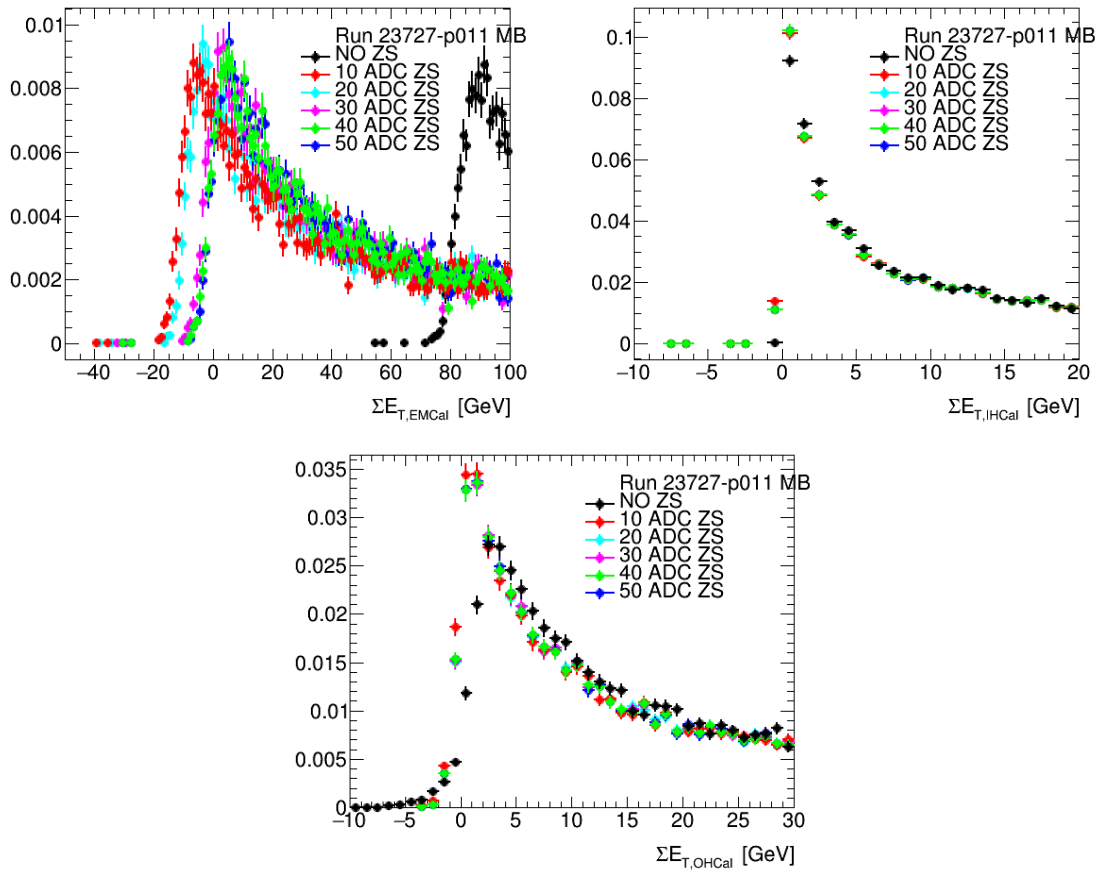


Figure 3.22: EMCAL, IHCAL and OHCal total total  $E_T$  distributions with ZS cross calibration factors applied for 5 different ZS thresholds. Plots made with ana.403 p011 production

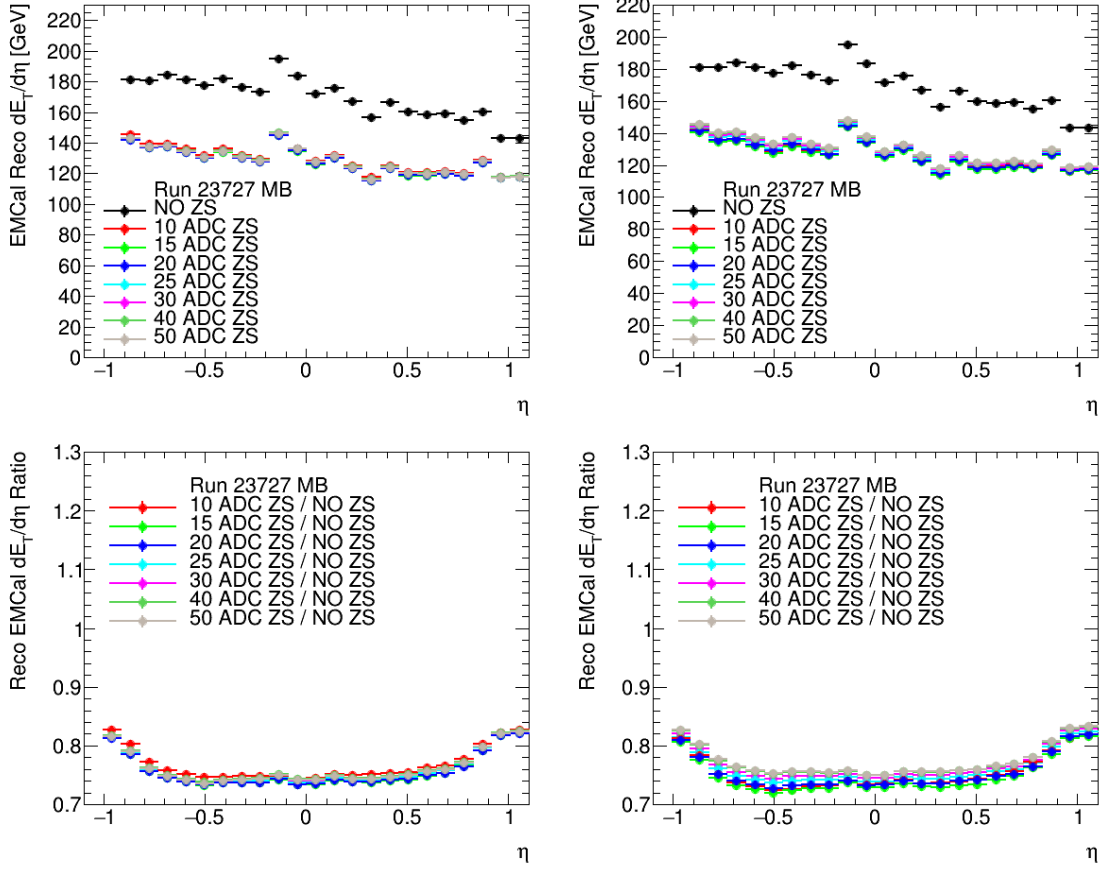


Figure 3.23: Comparison of reconstructed EMCAL  $dE_T/d\eta$  measurements (top) and ratios to full template fit EMCAL  $dE_T/d\eta$  (bottom) from beam data processed using ZS + template fit method for thresholds between 10 and 50 ADC with (left) and without (right) tower by tower ZS cross calibration factors applied.

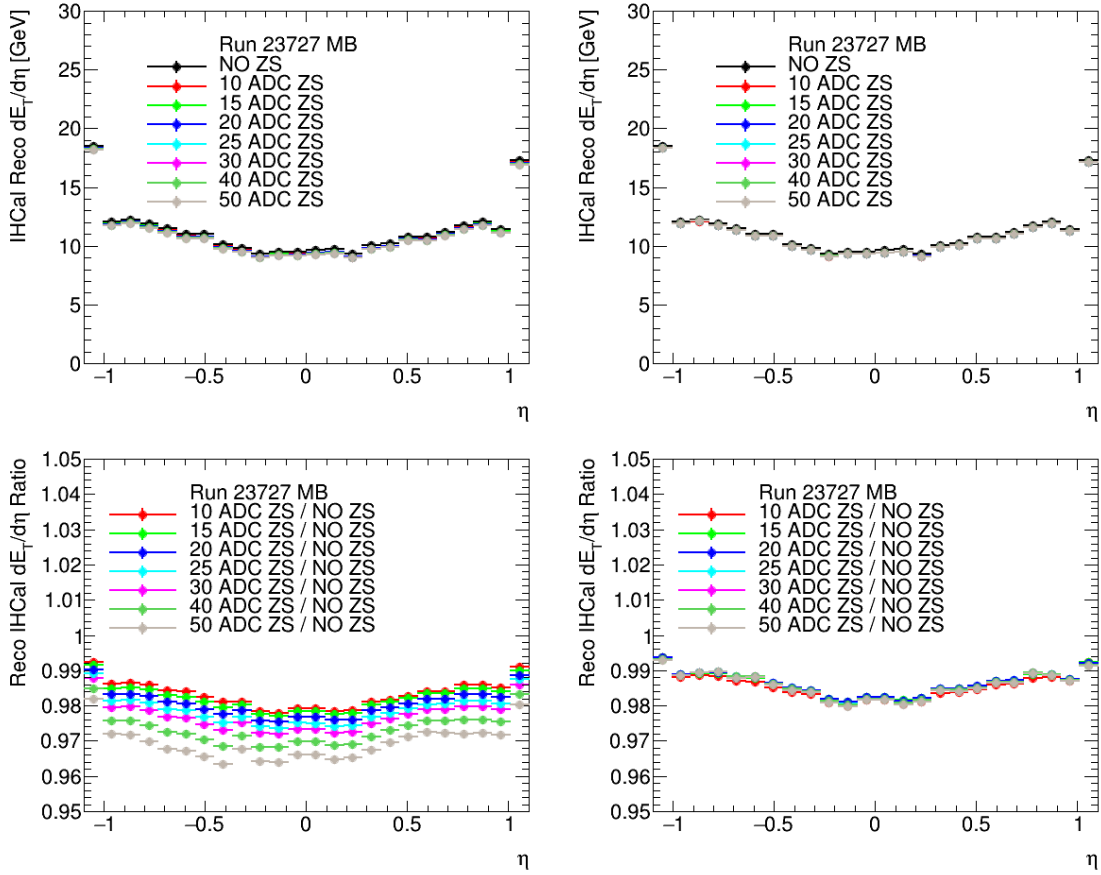


Figure 3.24: Comparison of reconstructed IHCAL  $dE_T/d\eta$  measurements (top) and ratios to full template fit IHCAL  $dE_T/d\eta$  (bottom) from beam data processed using ZS + template fit method for thresholds between 10 and 50 ADC with (left) and without (right) tower by tower ZS cross calibration factors applied.

level IHCAL  $dE_T/d\eta$  changes as a function of the ZS threshold. This is happening because real signal energies are underestimated when using the ZS method of waveform processing if the signal peak is not at exactly time sample 6. By raising the ZS threshold, the number of real signals processed with this ZS method that underestimates the tower's energy increases. Correcting for this effect by applying the ZS cross calibration factors, the reconstructed-level IHCAL  $dE_T/d\eta$  for all ZS thresholds is stable.

In Figure 3.25, the reconstructed-level OHCal  $dE_T/d\eta$  sees similar trends to the IHCAL: that applying any ZS threshold has a small effect on the reconstructed  $dE_T/d\eta$  and that in order to not underestimate the energy of waveforms processed by the ZS method and have calorimeter energies

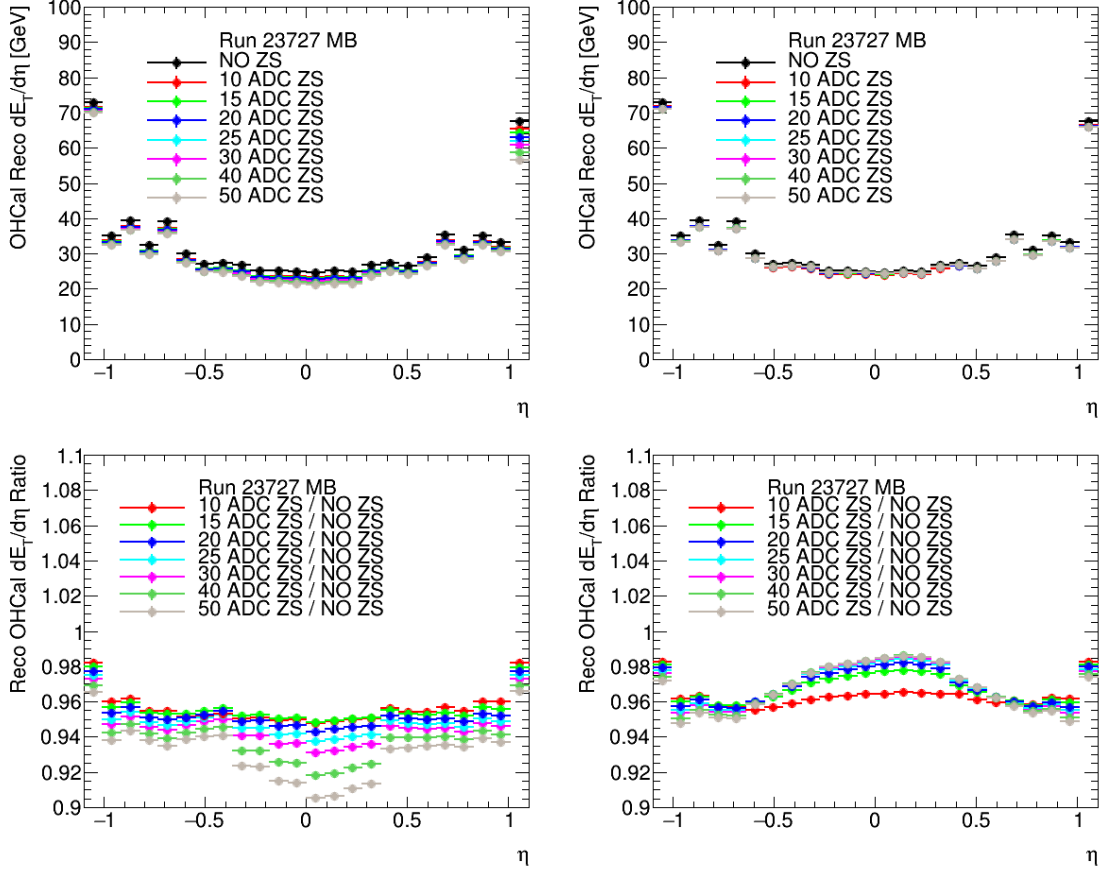


Figure 3.25: Comparison of reconstructed OHCal  $dE_T/d\eta$  measurements (top) and ratios to full template fit OHCal  $dE_T/d\eta$  (bottom) from beam data processed using ZS + template fit method for thresholds between 10 and 50 ADC with (left) and without (right) tower by tower ZS cross calibration factors applied.

be robust to ZS threshold, a tower by tower ZS cross calibration factor must be applied.

### ZS + template fit method on pedestal data

To ensure we are unbiasedly processing pedestal noise contributions in the ZS + template fit method, the ZS threshold scale was also applied to pedestal data. Waveforms from calorimeter pedestal data events are processed using the same ZS + template fit method for multiple ZS thresholds and then the reconstructed-level  $dE_T/d\eta$  from this pedestal data is investigated.

Figure 3.26 shows the EMCAL, IHCal and OHCal reconstructed-level  $dE_T/d\eta$  found using the ZS + template fit method from pedestal data taken during Run 2023. For all three calorimeters,

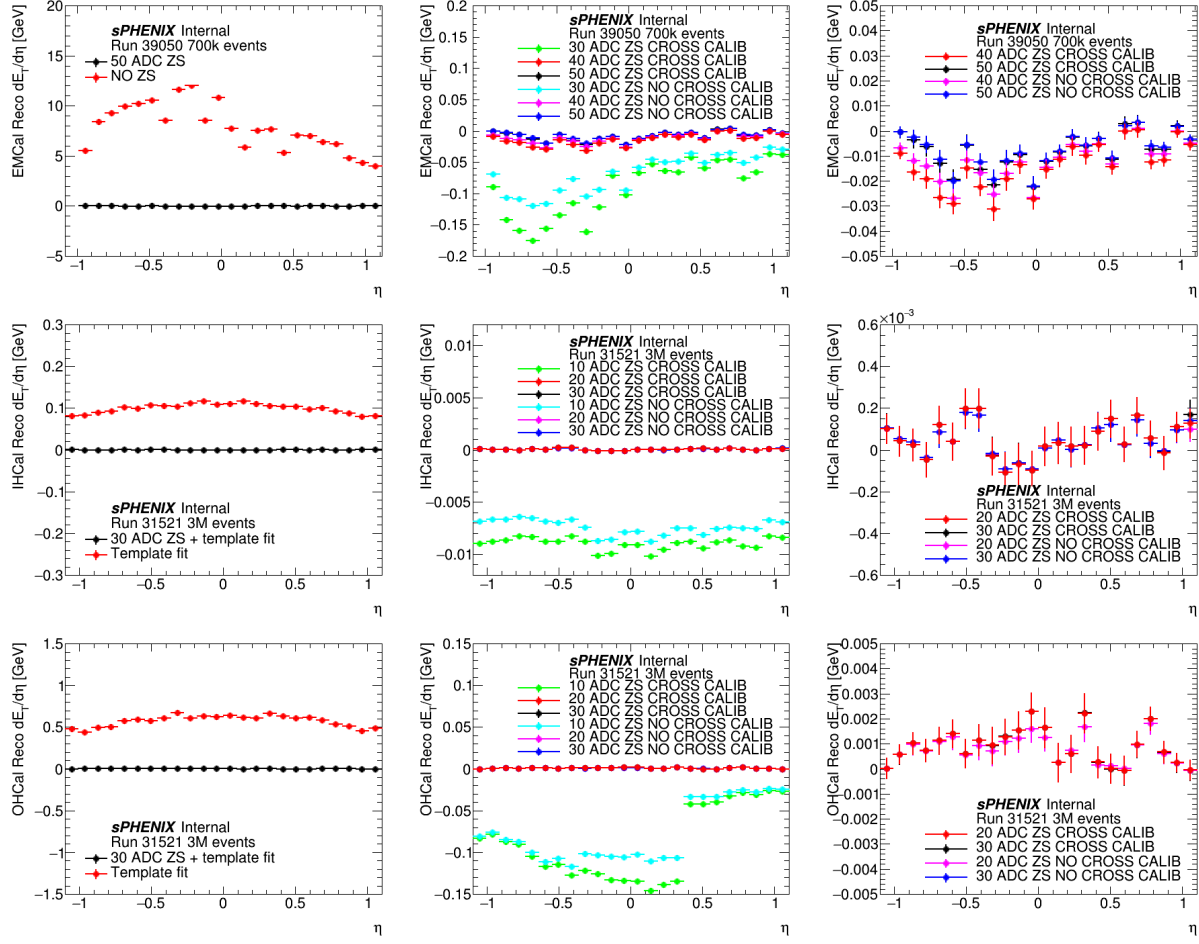


Figure 3.26: Comparison of reconstructed-level  $dE_T/d\eta$  from pedestal data processed using template fit only and ZS + template fit method for different ZS thresholds. Plots in right column are included to more clearly show the results included in the center column plots with values close to zero.

when processing the pedestal data only using the template fit, there is an overall positive value for the reconstructed-level  $dE_T/d\eta$ . However, when processing the IHCAL and OHCal pedestal data with the ZS + template fit method for a ZS threshold of 20 or 30 ADC, the reconstructed  $dE_T/d\eta$  in both the IHCAL and OHCal, a proxy for the overall energy contributions from noise, is consistent with 0. When processing the EMCAL pedestal data with the ZS + template fit method for a ZS threshold of 40 ADC, the reconstructed  $dE_T/d\eta$  in the EMCAL is less than 30 MeV for all  $\eta$  bins. These results combined with increased noise and radiation damage during Run 2024 informed the decision to process all calorimeter data from Run 2024 Au+Au ( $p+p$ ) data with the ZS + template fit method with ZS thresholds set to 100 (60) ADC for the EMCAL and 50 (30) ADC for each of the HCals.

## **Chapter 4: Transverse Energy Density Measurements in Au+Au Collisions**

## **Chapter 5: Underlying Event Measurements in p+p Collisions**

## **Chapter 6: Last Chapter before conclusion**

## **Conclusion or Epilogue**

Use this page for your epilogue or conclusion if applicable; please use only one of the titles for this page. Otherwise, you may delete it.

## References

- [1] M. Harrison, T. Ludlam, and S. Ozaki, “RHIC project overview,” *Nucl. Instrum. Meth. A*, vol. 499, pp. 235–244, 2003.
- [2] J. G. Alessi, D. Barton, E. Beebe, S. Bellavia, O. Gould, A. Kponou, R. Lambiase, R. Lockey, A. Mc너ney, M. Mapes, Y. Marneris, M. Okamura, D. Phillips, A. I. Pikin, D. Raparia, J. Ritter, L. Snydstrup, C. Theisen, and M. Wilinski, “The brookhaven national laboratory electron beam ion source for rhic,” *Review of Scientific Instruments*, vol. 81, no. 2, 02A509, Feb. 2010. eprint: [https://pubs.aip.org/aip/rsi/article-pdf/doi/10.1063/1.3292937/13929784/02a509\\_1\\_online.pdf](https://pubs.aip.org/aip/rsi/article-pdf/doi/10.1063/1.3292937/13929784/02a509_1_online.pdf).
- [3] M. Liu *et al.*, *A Monolithic-Active-Pixel-Sensor-based Vertex Detector (MVTX) for the PHENIX Experiment at RHIC*, Proposal submitted to the DOE Office of Science, Web, Feb. 2017.
- [4] H. S. Ko, “Mvtx: A maps vertex tracker for sphenix at rhic,” Mar. 2023, p. 073.
- [5] Z. Shi, *Heavy flavor physics at the sphenix experiment*, 2024. arXiv: 2401.11036 [nucl-ex].
- [6] C. W. Shih, G. Nukazuka, Y. Sugiyama, Y. Akiba, H. En’yo, T. Hachiya, S. Hasegawa, M. Hata, H. Imai, C. M. Kuo, M. Morita, I. Nakagawa, Y. Nakamura, G. Nakano, Y. Nimoto, R. Nouicer, M. Shibata, M. Shimomura, R. Takahama, K. Toho, M. Tsuruta, and M. Watanabe, *Beam test results of the intermediate silicon tracker for sphenix*, 2025. arXiv: 2509.00908 [physics.ins-det].
- [7] sPHENIX Collaboration, “sPHENIX Technical Design Report,” Tech. Rep., 2019.
- [8] H Klest, “Overview and design of the sphenix tpc,” *Journal of Physics: Conference Series*, vol. 1498, no. 1, p. 012 025, Apr. 2020.
- [9] S. Aune *et al.*, “The sPHENIX Micromegas Outer Tracker,” *Nucl. Instrum. Meth. A*, vol. 1066, p. 169 615, 2024. arXiv: 2403.13789 [physics.ins-det].
- [10] C. A. Aidala, S. Altaf, R. Belmont, S. Boose, D. Cacace, M. Connors, E. Desmond, J. Frantz, E. A. Gamez, N. Grau, J. S. Haggerty, A. Hodges, J. Huang, Y. Kim, M. D. Lenz, W. Lenz, N. A. Lewis, E. J. Mannel, J. D. Osborn, D. V. Perepelitsa, M. Phipps, R. Pisani, S. Polizzo, A. Pun, M. L. Purschke, C. Riedl, T. Rinn, A. C. Romero Hernandez, M. Sarsour, Z. Shi, A. M. Sickles, C. Smith, S. Stoll, X. Sun, E. Thorsland, F. Vassalli, X. Wang, and C. L. Woody, “Design and beam test results for the 2-d projective sphenix electromagnetic calorimeter prototype,” *IEEE Transactions on Nuclear Science*, vol. 68, no. 2, pp. 173–181, 2021.

- [11] C. A. Aidala, V. Bailey, S. Beckman, R. Belmont, C. Biggs, J. Blackburn, S. Boose, M. Chiu, M. Connors, E. Desmond, A. Franz, J. S. Haggerty, X. He, M. M. Higdon, J. Huang, K. Kauder, E. Kistenev, J. LaBounty, J. G. Lajoie, M. Lenz, W. Lenz, S. Li, V. R. Loggins, E. J. Mannel, T. Majoros, M. P. McCumber, J. L. Nagle, M. Phipps, C. Pinkenburg, S. Polizzo, C. Pontieri, M. L. Purschke, J. Putschke, M. Sarsour, T. Rinn, R. Ruggiero, A. Sen, A. M. Sickles, M. J. Skoby, J. Smiga, P. Sobel, P. W. Stankus, S. Stoll, A. Sukhanov, E. Thorsland, F. Toldo, R. S. Towell, B. Ujvari, S. Vazquez-Carson, and C. L. Woody, “Design and beam test results for the sphenix electromagnetic and hadronic calorimeter prototypes,” *IEEE Transactions on Nuclear Science*, vol. 65, no. 12, pp. 2901–2919, 2018.
- [12] M. A. et al., ‘‘PHENIX inner detectors,’’ *Nuclear Instruments and Methods in Physics Research Section A: Accelerators, Spectrometers, Detectors and Associated Equipment*, vol. 499, no. 2, pp. 549–559, 2003, The Relativistic Heavy Ion Collider Project: RHIC and its Detectors.
- [13] K. Ikematsu, Y. Iwata, K. Kaimi, M. Kaneta, T. Kohama, N. Maeda, K. Matsukado, H. Ohnishi, K. Ono, A. Sakaguchi, T. Sugitate, Y. Sumi, Y. Takata, M. Tanabe, and A. Yokoro, ‘‘A start-timing detector for the collider experiment phenix at rhic-bnl,’’ *Nuclear Instruments and Methods in Physics Research Section A: Accelerators, Spectrometers, Detectors and Associated Equipment*, vol. 411, no. 2–3, 238–248, Jul. 1998.
- [14] C Adler, A Denisov, E Garcia, M Murray, H Stroebele, and S White, ‘‘The rhic zero degree calorimeters,’’ *Nuclear Instruments and Methods in Physics Research Section A: Accelerators, Spectrometers, Detectors and Associated Equipment*, vol. 470, no. 3, pp. 488–499, 2001.
- [15] X. Wang and M. Gyulassy, ‘‘HIJING: A Monte Carlo model for multiple jet production in pp, pA, and AA collisions,’’ *Phys. Rev. D*, vol. 44, pp. 3501–3516, 11 1991.
- [16] C. Bierlich *et al.*, ‘‘A comprehensive guide to the physics and usage of PYTHIA 8.3,’’ *SciPost Phys. Codeb.*, vol. 2022, p. 8, 2022. arXiv: 2203.11601 [hep-ph].
- [17] M. R. Aguilar, Z. Chang, R. K. Elayavalli, R. Fatemi, Y. He, Y. Ji, D. Kalinkin, M. Kelsey, I. Mooney, and V. Verkest, ‘‘pythia8 underlying event tune for RHIC energies,’’ *Phys. Rev. D*, vol. 105, no. 1, p. 016011, 2022. arXiv: 2110.09447 [hep-ph].
- [18] S. A. et al., ‘‘GEANT4—a simulation toolkit,’’ *Nucl. Instrum. Meth. A*, vol. 506, pp. 250–303, 2003.
- [19] S. Navas *et al.*, ‘‘Review of particle physics,’’ *Phys. Rev. D*, vol. 110, no. 3, p. 030001, 2024.
- [20] D. Pagano, G. Bonomi, A. Donzella, A. Zenoni, G. Zumerle, and N. Zurlo, ‘‘EcoMug: An Efficient COsmic MUon Generator for cosmic-ray muon applications,’’ *Nuclear Instruments and Methods in Physics Research Section A: Accelerators, Spectrometers, Detectors and Associated Equipment*, vol. 1014, p. 165 732, 2021.

## **Appendix A: Experimental Equipment**

  Lorem ipsum dolor sit amet, consectetur adipiscing elit, sed do eiusmod tempor incididunt ut labore et dolore magna aliqua. Ut enim ad minim veniam, quis nostrud exercitation ullamco laboris nisi ut aliquip ex ea commodo consequat. Duis aute irure dolor in reprehenderit in voluptate velit esse cillum dolore eu fugiat nulla pariatur. Excepteur sint occaecat cupidatat non proident, sunt in culpa qui officia deserunt mollit anim id est laborum.

## **Appendix B: Data Processing**

  Lorem ipsum dolor sit amet, consectetur adipiscing elit, sed do eiusmod tempor incididunt ut labore et dolore magna aliqua. Ut enim ad minim veniam, quis nostrud exercitation ullamco laboris nisi ut aliquip ex ea commodo consequat. Duis aute irure dolor in reprehenderit in voluptate velit esse cillum dolore eu fugiat nulla pariatur. Excepteur sint occaecat cupidatat non proident, sunt in culpa qui officia deserunt mollit anim id est laborum.